

HST/STIS High Resolution Echelle Spectra of α Centauri A (G2 V)[★]

Isabella Pagano¹, Jeffrey L. Linsky², Jeff Valenti³, and Douglas K. Duncan⁴

¹ INAF, Catania Astrophysical Observatory, via Santa Sofia 78, 95125 Catania, Italy
e-mail: ipa@ct.astro.it

² JILA, University of Colorado and NIST, Boulder, CO 80309-0440, USA
e-mail: jlinsky@jila.colorado.edu

³ Space Telescope Science Institute, 3700 San Martin Dr. Baltimore, MD 21218, USA
e-mail: valenti@stsci.edu

⁴ Department of Astrophysical and Planetary Sciences, University of Colorado, Boulder, CO 80309-0389, USA
e-mail: dduncan@colorado.edu

Received 2003, Jun 25; accepted 2003, Oct 09

Abstract. We describe and analyze HST/STIS observations of the G2 V star α Centauri A (α Cen A, HD 128620), a star similar to the Sun. The high resolution echelle spectra obtained with the E140H and E230H gratings cover the complete spectral range 1133–3150 Å with a resolution of 2.6 km s^{−1}, an absolute flux calibration accurate to ±5%, and an absolute wavelength accuracy of 0.6–1.3 km s^{−1}. We present here a study of the E140H spectrum covering the 1140–1670 Å spectral range, which includes 671 emission lines representing 37 different ions and the molecules CO and H₂. For α Cen A and the quiet and active Sun, we intercompare the redshifts, nonthermal line widths, and parameters of two Gaussian representations of transition region lines (e.g., Si, C), infer the electron density from the O intersystem lines, and compare their differential emission measure distributions. One purpose of this study is to compare the α Cen A and solar UV spectra to determine how the atmosphere and heating processes in α Cen A differ from the Sun as a result of the small differences in gravity, age, and chemical composition of the two stars. A second purpose is to provide an excellent high resolution UV spectrum of a solar-like star that can serve as a proxy for the Sun observed as a point source when comparing other stars to the Sun.

Key words. Stars: individual (α Cen A) — stars: chromospheres — ultraviolet: stars — ultraviolet: spectra — line: identification — line: profiles

1. Introduction

Our knowledge and understanding of phenomena related to magnetic activity in late-type stars is based largely on the analysis of observations of the Sun obtained with high spatial, spectral and temporal resolution. In particular, the different heating rates and emission measure distributions of stellar chromospheres and transition regions can be understood by comparing stellar UV spectra with corresponding solar spectra. However, as strange as this may at first appear, we lack a true “reference spectrum” for the Sun observed as a star for such comparisons. In fact, the existing solar UV spectra provided by instruments on the *Solar Maximum Mission* (SMM) and the *Solar and Heliospheric Observatory* (SOHO) typically have moderate to high spectral resolution, but do not represent a full disk average, have uncertain wavelength and absolute flux calibrations, and consist of a stitching together of

many small parts of the UV spectrum obtained at different times. Table 1 summarizes the instrumental characteristics of these data sets. For example, the UV spectral atlas obtained with the *High Resolution Telescope and Spectrograph* (HRTS) rocket experiment (Brekke, 1993b) and the recent UV spectral atlas obtained with the *Solar Ultraviolet Measurements of Emitted Radiation* (SUMER) instrument on the *Solar and Heliospheric Observatory* (SOHO) (Curdt et al., 2001) have high spectral resolution, but do not provide the solar irradiance (the Sun viewed as a point source) for direct comparison with stellar spectra. On the other hand, spectra of the Sun as a point source obtained with the *Solar-Stellar Irradiance Comparison Experiment* (SOLSTICE) instrument on the *Upper Atmospheric Research Satellite* (UARS) (Rottman, Woods, & Sparn, 1993), the *EUV Grating Spectrograph* (Woods & Rottman, 1990), and the *Coronal Diagnostic Spectrometer* (CDS) on SOHO (Brekke et al., 2000) do not have sufficient spectral resolution to resolve the line profiles.

Table 1 Ultraviolet spectral atlases of the Sun and α Cen A

Instrument Used	Spectral Range (Å)	Spectral Resolution	Solar Location	Flux Calibration	Reference
HRTS	1190–1730	0.05Å	quiet Sun	$\pm 30\%$	(1)
			active Sun		(1)
UVSP/SMM	1150–3600	$\sim 100,000$	disk center		(2)
SOHO/SUMER	465–1610	17,770–38,300	disk center	$\pm 20\%$	(3)
			sunspot, CH	$\pm 20\%$	(3)
SOHO/CDS	150–800	0.3–0.6Å	slit on disk	not given	(4)
	307–632	0.3–0.6Å	Sun-as-a-star	15–45%	(5)
SOLSTICE/UARS	1190–4200	1–2 Å	Sun-as-a-star	$\pm 5\%$	(6)
rocket EGS	300–1100	2Å	Sun-as-a-star	$\pm 15\%$	(7)
STIS E140H	1140–1670	114,000	α Cen A	$\pm 5\%$	(8)

(1) Brekke (1993b), (2) Shine & Frank (2000), Woodgate et al. (1980), (3) Curdt et al. (2001),

(4) <http://solg2.bnsc.rl.ac.uk/atlas/atlas.shtml>, (5) Brekke et al. (2000), (6) Rottman, Woods, & Sparn (1993),

(7) EUV Grating Spectrograph, Woods & Rottman (1990), (8) Leitherer et al. (2001), Bohlin, Dickinson, & Calzetti (2001).

One way to obtain a close approximation to a high resolution spectrum of the whole Sun observed as a point source with excellent S/N, absolute flux calibration, and wavelength accuracy is to observe a bright star with very similar properties to the Sun. We have done this with the *Space Telescope Imaging Spectrograph* (STIS) instrument on HST (Woodgate et al., 1998), obtaining a very high S/N and high resolution ($R = \lambda/\Delta\lambda \approx 114,000$) spectrum of the star α Cen A, a nearby ($d=1.34$ pc) twin of the Sun with the same spectral type (G2 V). Although there are some small differences in effective temperature and metal abundances between α Cen A and the Sun (see below), this STIS spectrum of α Cen A can be considered the best available “reference spectrum” for the Sun viewed as a star, because it is a full disk average, has excellent wavelength and flux calibration (Bohlin, Dickinson, & Calzetti, 2001), and covers the entire 1130–3100 Å UV range with high S/N and within a short period of time.

α Cen AB (G2 V + K1 V) is the binary system located closest to the Earth ($d=1.34$ pc). It shows an eccentric orbit ($e=0.519$) with a period of almost 80 years (Pourbaix et al., 2002). Actually α Cen is a triple star system. The third member of the system, α Cen C or Proxima Cen, is a M5.5 Ve flare star ($V=11.05$) about 12 000 AU distant from α Cen and only $d=1.29$ pc from the Sun (Perryman et al., 1997). Thanks to the high apparent brightness ($V=-0.01$ and $V=1.33$ for the A and B component, respectively) and large parallax of the α Cen stars, their surface abundances, other stellar properties, and astrometric parameters are among the best known of any star except the Sun. Guenther & Demarque (2000), Morel et al. (2000), and Pourbaix et al. (2002) have reviewed recent determinations of the physical characteristics of α Cen AB. According to Morel et al. (2000) and references therein, α Cen A has nearly the same surface temperature of the Sun ($T_{\text{eff}}=5790\pm 30$ K), slightly lower gravity than the Sun ($\log g=4.32\pm 0.05$, i.e. $0.76 g_{\odot}$), and a mass of $1.16\pm 0.03 M_{\odot}$ - which is probably an upper limit, given different estimates reported in the literature starting from $1.08 M_{\odot}$ (Guenther & Demarque, 2000). The same authors give a metal overabundance of ~ 0.2 dex with respect to the Sun, but similar Li and Be abundances to the Sun. In Table 2 we list the α Cen A abun-

dances used in this paper, which were compiled from Feltzing & Gonzalez (2001) and Morel et al. (2000). The age of α Cen A is controversial: Morel et al. (2000) derive an age in the range 2.7–4.1 Gyr depending on the adopted convection model, while Guenther & Demarque (2000) estimate an age in the range 6.8–7.6 Gyr. One could argue that α Cen A is younger than the Sun on the basis that it is formed of metal enriched material, but the larger radius and lower gravity compared to the Sun argue that the star is more evolved and somewhat older than the Sun, even considering its somewhat larger mass. A closer analog to the Sun is 18 Sco ($V=5.50$), but this star is too faint to get high S/N high resolution UV spectra with STIS.

Table 2 Abundances of α Cen A in log units.

Atom	Abund.	Ref.	Atom	Abund.	Ref.
H	12.00	1	S	7.33	3
He	10.93	1	Cl	5.50	1
Li	1.30	2	Ar	6.40	3
Be	1.40	3	K	5.12	3
B	2.55	3	Ca	6.58	1
C	8.72	1	Sc	3.42	1
N	8.22	1	Ti	5.27	1
O	9.04	1	V	4.23	1
F	4.56	3	Cr	5.92	1
Ne	8.08	3	Mn	5.62	1
Na	6.33	3	Fe	7.75	1
Mg	7.58	3	Co	5.20	1
Al	6.71	1	Ni	6.55	1
Si	7.82	1	Cu	4.46	4
P	5.45	3	Zn	4.85	4

References:

1) Feltzing & Gonzalez(2001);

2) Morel et al.(2000);

3) Solar values from Grevesse & Sauval (1998);

4) scaled from the Fe abundance.

α Cen has been extensively studied in the ultraviolet by IUE. Jordan et al. (1987) used IUE data to create simple one-dimensional models of the atmospheric structure of the two stars. Hallam et al. (1991) have studied the rotational modu-

lation of the most prominent lines in IUE spectra of α Cen A and found a rotation period of about 29 d. This is consistent with the Boesgaard & Hagen (1974) estimate that the α Cen A rotation period is 10% larger than the solar one, but is larger than the ~ 22 d rotation period derived from the 2.7 ± 0.7 km s $^{-1}$ rotational velocity measured by Saar & Osten (1997), assuming a radius of $\sim 1.2 R_{\odot}$ and an orbital inclination of $\sim 79^{\circ}$. Ayres et al. (1995) have studied the time variability of the most prominent UV lines of α Cen A and B during about 11 years of observations. While a clear evidence of a solar-like activity cycle was found for α Cen B, UV line fluxes from α Cen A do not give any clear indication for an activity cycle.

In this paper we report on the α Cen A spectrum recorded with the E140 grating by *HST/STIS* between 1140–1670 Å, while the analysis of the E230H spectrum (1620–3150 Å) will be published in a forthcoming paper. Information on data acquisition and reduction are provided in Section 2, the spectral line identification and the analysis of interesting lines are presented in Section 3. A detailed comparison of our *STIS* α Cen A spectrum, with the *SOHO/SUMER* (Curd et al., 2001) and the *SMM/UVSP* (Shine & Frank, 2000) spectra of the Sun is given in Section 5. Then, we derive the α Cen A transition region electronic densities (Section 6), and emission measure distribution (Section 7). In Section 8 we call the reader’s attention on some absorption features present in high excitation lines, and give our conclusions in Section 9.

2. The α Cen A Data

The E140H spectrum of α Cen A was acquired on 1999 Feb 12 with 3 exposures of 4695 s each, centered at 1234, 1416, and 1598 Å, respectively. The E140H mode ensures an average dispersion of $\lambda/228,000$ Å per pixel, which corresponds to a resolving power of 2.6 km s $^{-1}$. The E140H grating is used with the FUV-MAMA detector, which we operated in TIME-TAG mode. We used the 0.2×0.09 arcsec aperture.

The data were reduced using the *STIS* Science Team’s IDL-based software, CALSTIS (Version 6.6). CALSTIS performs a variety of functions including flat fielding, assignment of statistical errors, compensation for the Doppler shifts induced by the spacecraft’s motion in orbit, conversion of counts to count rates, dark-rate image subtraction, and the removal of data from bad/hot pixels. Wavelength calibration was carried out assuming the post launch echelle dispersion coefficients and a dispersion coefficient correction for the Monthly MSM offsets released to the *STIS* Science Team on 1999 September (Lindler, 1999b). The on-board Pt lamp spectra taken in association with the science observations were used to measure zero point adjustments. For the echelle observations, CALSTIS computes a wavelength offset for each spectral order. The adopted offset is the median of these offsets. As a check for the success of the algorithm used, we have verified that the measured offsets are all within one pixel of the median offset. As a further check on the accuracy of the wavelength scale, we measured the centroids of emission lines recorded in adjacent orders, and found that the results agree to within less than 1 pixel. The nominal absolute wavelength accuracy is 0.5–1 pixel (i.e. 0.6 – 1.3 km s $^{-1}$) (Leitherer et al., 2001).

CALSTIS outputs a file containing wavelength, flux, and error vectors, which is used in all subsequent processing. To remove the effects of scattered light that are important near the Ly- α line, we used the IDL ECHELLE_SCAT routine (Lindler, 1999a) in the *STIS* Science Team’s software package. This routine uses the first estimate of the spectrum and a scattering model of the spectrograph to determine the intensity of the scattered light and to estimate what the spectrum plus scattered light image should look like. Comparison of this calculated spectrum with the observations yields differences that indicate the errors in the first estimate of the spectrum. This spectrum is then corrected and the process is iterated until acceptable agreement is obtained between the prediction and the observed image.

After correction for scattered light, the spectrum was then analyzed using software packages written in IDL. We used routines of the ICUR fitting code¹, adapted to handle our *STIS* data, which perform multi-Gaussian fits to the line profiles using Bevington’s (1969) CURFIT algorithm. To correct for instrumental broadening, we convolved each proposed fit to an emission line profile with the instrumental line spread function (LSF), which was assumed to be a Gaussian with the nominal width ranging from ~ 1.2 pixel at 1200 Å to ~ 1 pixel at 1700 Å (Leitherer et al., 2001), as is appropriate for lines which are much broader than the width of the LSF.

3. Results

3.1. The Ultraviolet Spectrum of α Cen A

In Figure 1 we show the E140H spectrum of α Cen A. We have measured a total of 662 emission features of which 77 are due to blends of two or more lines, 71 are due to unidentified transitions, and 514 are identified as due to single emission lines. Taking into account the 157 lines identified in blended features, we find a total of 671 emission lines in this spectrum. In Table 3 we list all the ions that have been identified. Most of these lines are due to Si, Fe, C, which together contribute 441 lines, but S and Ni are each represented by more than 30 lines.

Table 4², lists the line identifications, laboratory and measured wavelengths, radial velocity shifts corrected for the stellar radial velocity of -23.45 km s $^{-1}$, computed using the orbital parameters and ephemeris given by Pourbaix et al. (2002), line full-widths at half-maxima (FWHM), and line fluxes. The laboratory wavelengths listed in Table 4 are from Sandlin et al. (1986), unless otherwise noted in the table. We used Gaussian fits to the line profiles to measure wavelengths, FWHM, and fluxes for single or blended emission lines which do not show central reversals. For the lines which have interstellar absorption components or central reversals, i.e. the most intense optically thick chromospheric lines of C, O, Si, and C, we instead integrated the flux contained in a suitable wavelength interval and tabulated the FWHM of the observed profile. In

¹ ICUR (<http://sbast3.ess.sunysb.edu/fwalter/ICUR/icur.html>) is a general purpose screen-oriented data analysis program written in IDL for manipulating and analyzing one dimensional spectra. It is distributed to the public by the authors (F.M. Walter and J.E. Neff).

² Table 4 is also available at the CDS

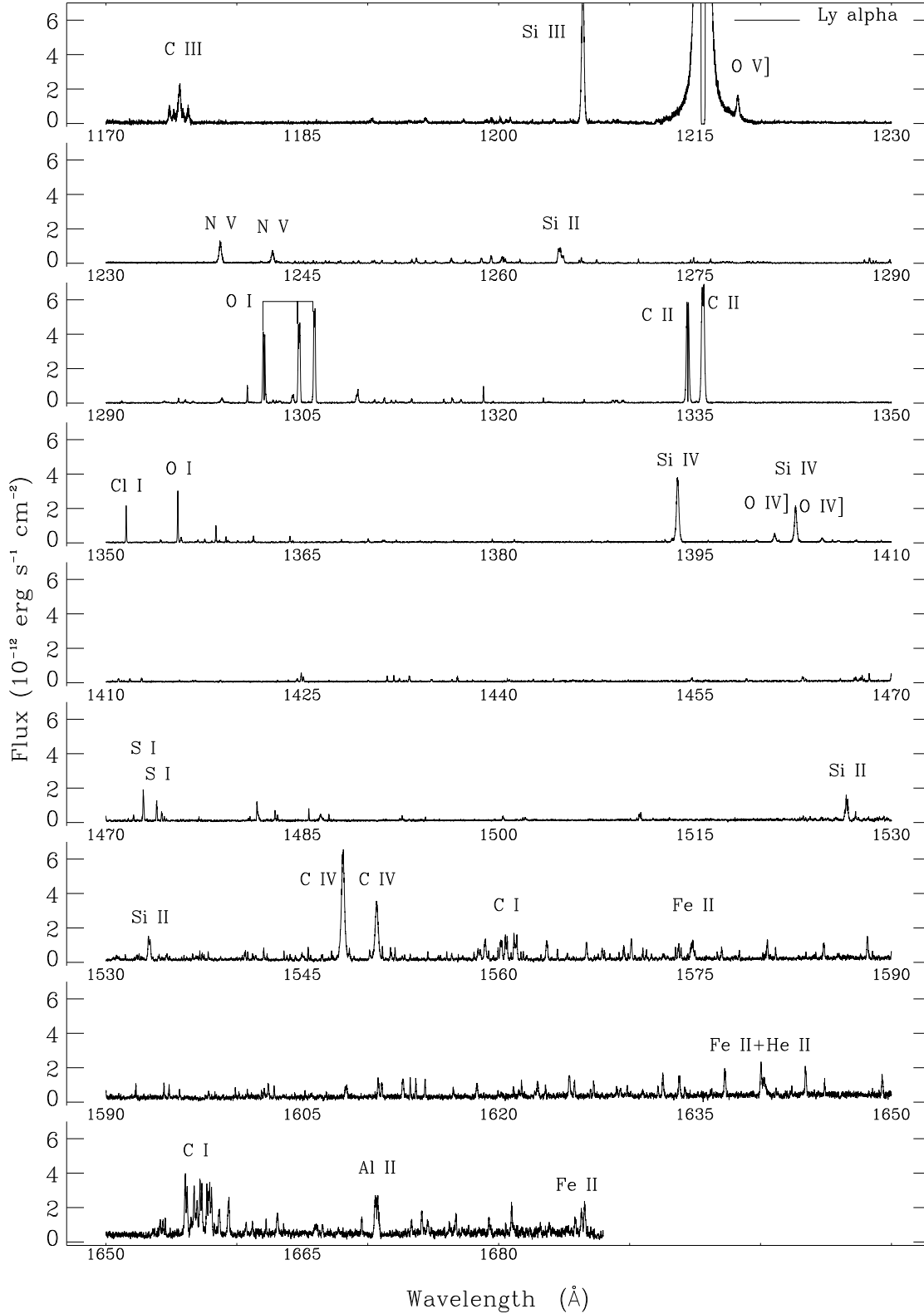


Fig. 1 The E140H spectrum of α Cen A obtained on 1999 Feb 12. Important spectral features are marked.

Table 4 these lines are indicated with “CR” in the *Notes* column.

The strongest transition region lines show broad wings, and therefore do not have a Gaussian profile. For these lines, we list

in Table 4 the line centroid, the FWHM of the observed profile and the flux integrated in a suitable wavelength interval. The analysis of these lines is reported in Section 3.3.

Table 3 Lines detected in the STIS E140H spectrum of α Cen A.

Ion	No. of lines		Ion	No. of lines	
	Total	Blended		Total	Blended
Si I	155	46	O IV	5	1
Fe II	144	20	Ca II	4	3
C I	142	32	Cl I	3	
S I	55	6	S II	3	
Ni II	34	8	S III	3	1
Si II	17	4	S IV	3	1
H ₂	14	11	C IV	2	
N I	13	6	Fe V	2	
CO	11	6	N V	2	
C III	8	1	O III	2	
Fe IV	8	1	O V	2	
Si III	7	2	Si IV	2	
O I	6	1	S V	2	1
C II	6	4			
P I	5				

1 line each for Al II, Al IV, Ca VII, Cl II, Cr II,
Fe XII, H I, He II, and N IV
1 line in blended features for P II, and Si VIII

Absorption features due to the interstellar medium have been measured in a number of lines originating in transitions from the ground level. Such lines are indicated with “ISM” in Table 4 (column *Notes*). They will be discussed in a separate paper, together with the derived properties of the interstellar medium along this line of sight.

Several intersystem lines are present in the spectrum of the α Cen A, including the O UV 0.01 intercombination multiplet $2s^2 2p^2 P^0_J - 2s 2p^2 \ ^4P_J$, that are diagnostics of electron density (cf. Del Zanna, Landini, & Mason 2002; Brage et al. 1996, and references therein), the N line at 1486 Å, and the O line at 1666 Å. We have used these lines to measure densities in the α Cen A chromosphere and transition region as discussed in Section 6.

3.2. Comments on individual line identifications

According to the NIST database, we have identified the broad feature near 1199 Å as S (see Figure 2a). However, it is possible that other unidentified lines are present. In fact, the flux measured at 1199.08 Å seems too large to be consistent with the differential emission measure distribution derived in Section 7.

The chromospheric Ly α emission line is altered greatly by the superimposed narrow, weak deuterium (D I) interstellar absorption and by very broad, saturated hydrogen (H I) interstellar, heliospheric, and astrospheric absorption, and by geocoronal emission. The Ly α line flux given in Table 4 was estimated by fitting a Gaussian to the wings of the line profile, disregarding the central part of the line, which is strongly affected by ISM absorption and geocoronal emission, and including a second Gaussian to account for the Deuterium absorption. This is a very rough estimate of the Ly α flux. We refer to the Linsky & Wood (1996) and Wood et al. (2001) papers for reliable estimates of the intrinsic Ly α in α Cen A.

The two O lines that we have measured in the α Cen A STIS spectrum have radial velocities differing by about 1.8 km s^{-1} , with the 1218 Å line less red-shifted than the line at 1371 Å. On the Sun, the 1371 Å line has a Doppler shift of $\sim 5 \text{ km s}^{-1}$ greater than the 1218 Å line, but Brekke (1993a) concluded that such a difference between the two lines can be explained only by an error in the adopted laboratory wavelength of the O 1218 Å line, which is an intersystem line and thus difficult to measure in the laboratory. However, if this were the case, adoption of the wavelength 1218.325 Å suggested by Brekke (1993a) as the laboratory wavelength, leads to a significant difference (2.8 km s^{-1}) in the opposite sense. We suggest that the main reason of the slight wavelength disagreement, even on the Sun, can be attributed to the difficulty in measuring the wavelength of the O 1218 Å line (see Figure 2b) in the sloping wing of the Ly α line. The O line at 1371 Å (see Figure 2c) shows a double peak with an apparent central reversal. We know of no explanation for this effect as the line is unlikely to be optically thick and thus self-reversed, and interstellar absorption is also unlikely.

A blow-up of the region with a complex feature located near 1241.8 Å is shown in Figure 3. The feature is noisy, but its double-peak structure is preserved even after smoothing with a boxcar average of width as large as 13 pixels. We have therefore fitted the profile with two Gaussians, and identified the two lines as the S 1241.9 Å and Fe 1242 Å lines. Since the Fe line is formed at temperature $\log T = 6.13$, its predicted thermal width is $\sim 33 \text{ km s}^{-1}$. We have frozen the line width of the Fe line to its thermal width, and derived a flux of $6.3 \times 10^{-15} \text{ erg s}^{-1} \text{ cm}^{-2}$. An a-posteriori check for the accuracy of our measured flux is given by the excellent agreement between the emission measure derived by using this line at $\log T = 6.13$ and the emission measure derived at temperatures $\log T = 6.04$ and 6.3 from Chandra spectra (Raassen et al., 2003) (cf. Section 7).

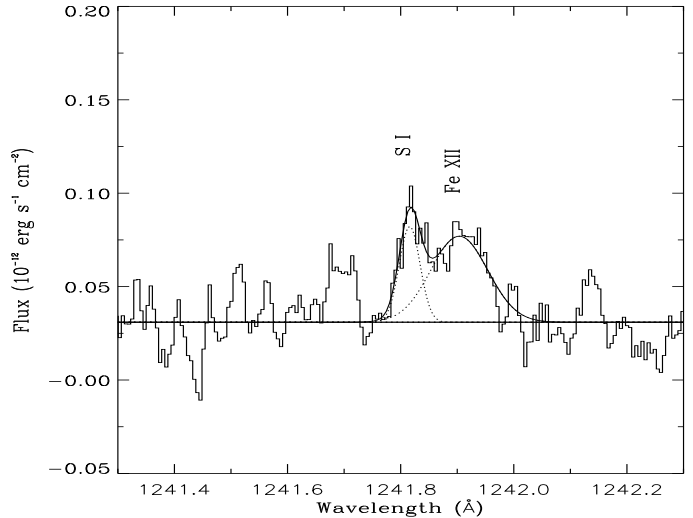


Fig. 3 A double-peak structure identified as the S at 1241.9 Å and the Fe 1242 Å lines.

The weak emission feature observed in solar spectra at $\sim 1356.88 \text{ Å}$ was tentatively attributed to the S line at 1357.0 Å

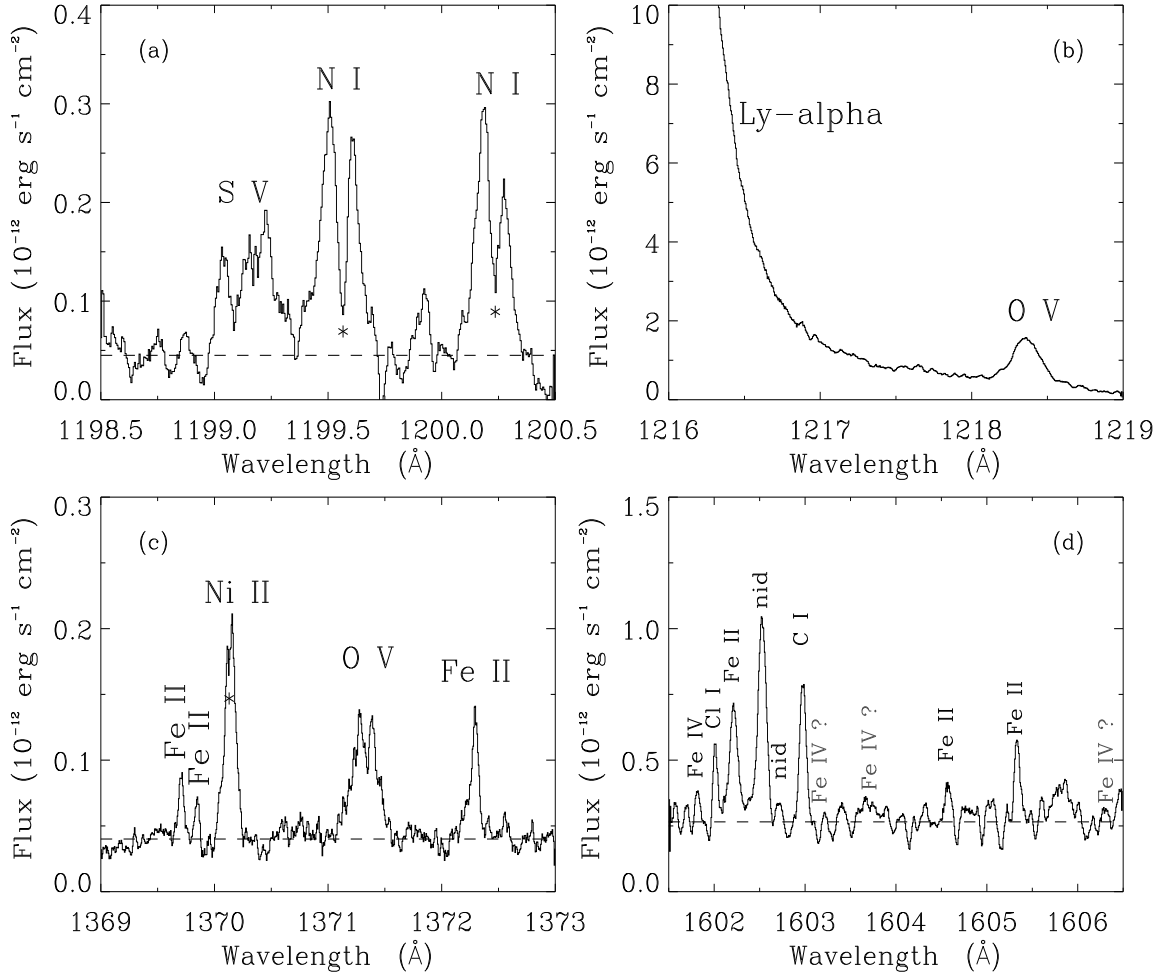


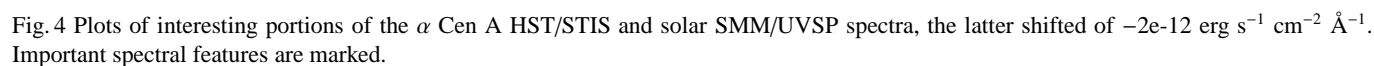
Fig. 2 Blow-up of the regions containing the S λ 1199.134 Å line (panel a), the O λ 1218 & 1371 Å lines (panels b and c), and the Fe quadruplet between 1601.5 and 1606.5 Å (panel d). Of this quadruplet we could measure only the 1602 Å line. Light-ink labels in panel d indicate the positions of the missed Fe lines. The symbol * in panels a and c marks the absorption components due to the interstellar medium. In all of the panels the wavelength scale has been shifted according to the stellar radial velocity.

by Feldman et al. (1975). Its laboratory wavelength makes this line slightly blue-shifted, in contrast with the expectation (cf. Section 4), therefore we can argue that either the identification is wrong or the laboratory wavelength given by Feldman et al. (1975) is inaccurate.

We have measured the Fe line at 1602 Å that belongs to a multiplet of four lines. A careful inspection of the spectrum shows slight flux increments at the wavelengths corresponding to the 1603.181, and 1603.730 Å Fe lines, which, however, are below our detection limit as shown in Figure 2 (panel d), but we do not find any appreciable emission feature corresponding to the fourth line of this multiplet at 1606.333 Å. While all of the Fe lines have been identified in the Kelly (1982) line database, no Fe lines have been identified in the solar spectrum analyzed by Sandlin et al. (1986). We have inspected the solar *SMM/UVSP* spectrum (Shine & Frank, 2000) to look for Fe lines, but even the strongest line measured in the α Cen A *STIS* spectrum at \sim 1656 Å is missing in the solar spectrum, as shown in the left-bottom panel of Figure 4.

3.3. The Broad Wings of the Transition Region Emission Lines

As shown by Wood et al. (1997), the strongest transition region emission lines of α Cen A have profiles with broad wings. We find that broad wings are present in the Si λ 1206 Å, N λ 1238 Å, Si λ 1393 & 1402 Å, and C λ 1548 & 1502 Å line profiles. For these lines we used one narrow Gaussian component (NC) to fit the line core and one broad Gaussian component (BC) to fit the broad wings (see Figure 5). This bi-modal structure of the transition region lines is typically observed for several RS CVn-type stars (i.e., Capella and HR 1099), main sequence type stars (i.e., AU Mic, Procyon, α Cen A, and α Cen B), and the giants 31 Com, β Cet, β Dra, β Gem, and AB Dor (Linsky & Wood, 1994; Linsky et al., 1995; Pagano et al., 2000). Wood et al. (1997) showed that the narrow components can be produced by turbulent wave dissipation or Alfvén wave heating mechanisms, while the broad components, that resemble the explosive events on the Sun, are diagnostics for microflare heating. Analysis of *SUMER* data led Peter (2001) to propose an alternative explanation for the broad Gaussians,



which he calls the “tail component”, seen in lines formed at temperatures between 50,000 and 300,000 K in the chromospheric network. He argues that the tail component originates in coronal funnels that magnetically connect the lower transition region with the corona, and the broadening is by passing magneto-acoustic waves.

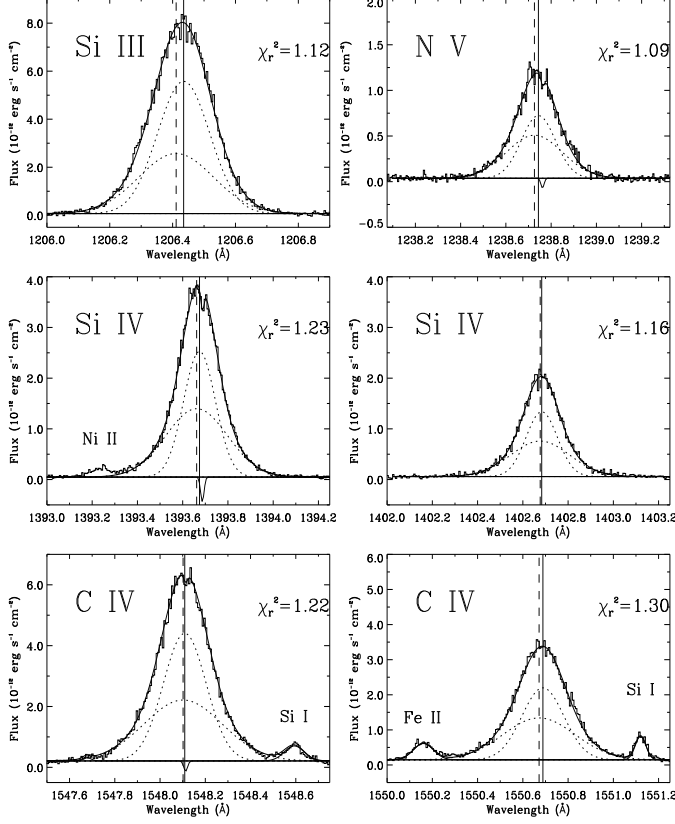


Fig. 5 The Si III, N V, Si IV, and C IV line profiles. The narrow and broad dashed lines indicate the narrow and broad Gaussian components, respectively, required to best fit the broad wings of these transition region lines. The vertical solid and dashed lines indicate the centroids of the narrow and broad Gaussians, respectively.

Table 5 lists the parameters resulting from our multi-Gaussian fits³. Both the narrow and broad components are redshifted with respect to the stellar chromosphere, whose rest velocity is determined by the mean velocity of 80 selected Si I lines as discussed in Section 4. The narrow components show larger redshifts as is seen in solar data (Peter, 2001). This effect was also noticed by Wood et al. (1997), who analyzed the Si IV 1393 Å line in GHRS/HST spectra of α Cen A.

The broad and narrow Gaussian components have comparable intensity as the flux-weighted mean ratio between the flux in the broad component and the total flux is 0.46 ± 0.05 . This ratio is typical for the most active stars studied by Wood et al. (1997), and it appears to be independent of the activity level of the star.

³ For the fits of N V 1238 Å, Si IV 1393 Å, and C IV 1548 Å, a third Gaussian component was used to account for the absorption feature possibly originating in the intervening interstellar medium.

Table 5 Parameters derived from the multi-Gaussian fits to the transition region emission lines of α Cen A which show broad wings. Flux is in units of 10^{-15} .

N	C			
I		v_{rad} (km s ⁻¹)	FWHM (km s ⁻¹)	Flux (erg s ⁻¹ cm ⁻²)
Si III 1206.510		+5.2± 0.4	48.7± 0.4	1148.2± 13.7
N V 1238.821		+5.1± 0.8	42.8± 2.4	129.5± 9.0
Si IV 1393.755		+6.5± 0.2	35.7± 0.5	437.9± 6.8
Si IV 1402.770		+5.4± 0.3	34.8± 0.7	221.8± 4.4
C IV 1548.187		+8.8± 0.2	43.2± 0.4	996.0± 11.5
C IV 1550.772		+7.8± 0.4	42.3± 1.5	478.2± 22.9
Flux-weighted				
average		+6.8± 1.5	43.4± 4.7	...

B	C			
I		v_{rad} (km s ⁻¹)	FWHM (km s ⁻¹)	Flux (erg s ⁻¹ cm ⁻²)
Si III 1206.510		-0.7± 0.7	69.6± 0.4	745.4± 13.7
N V 1238.821		+0.9± 1.2	70.4± 2.4	187.8± 7.4
Si IV 1393.755		+3.8± 0.3	69.1± 0.5	461.1± 6.8
Si IV 1402.770		+3.9± 0.6	65.6± 0.8	228.8± 4.4
C IV 1548.187		+7.4± 0.4	78.8± 0.6	867.8± 11.5
C IV 1550.772		+4.5± 0.6	72.1± 1.7	474.0± 32.5
Flux-weighted				
average		+3.6± 3.1	72.4± 4.4	...

C	F	R	V	S	χ_r^2
	F_{BC}/F_{tot}		$(v_{NC} - v_{BC})$		
Si III 1206.510	0.39± 0.01		+5.9± 0.8		1.12
N V 1238.821	0.59± 0.03		+4.3± 1.4		1.08
Si IV 1393.755	0.51± 0.01		+2.7± 0.4		1.15
Si IV 1402.770	0.51± 0.01		+1.5± 0.7		1.36
C IV 1548.187	0.47± 0.01		+1.4± 0.5		1.17
C IV 1550.772	0.50± 0.04		+3.3± 0.7		1.30
Flux-weighted					
average	0.46± 0.05		+3.4± 1.8		

The flux-weighted average of the FWHMs are 43.4 ± 4.7 , and 72.4 ± 4.4 km s⁻¹ for the narrow and broad components, respectively. By comparison, explosive events on the Sun produce transition region lines as broad as FWHM~ 100 km s⁻¹ (Dere et al., 1989).

4. Turbulent velocity and velocity shifts with line formation temperature

Lines of the same ion generally form at nearly the same temperature in a collisional ionization equilibrium plasma. Therefore, for most ions we use all the measured lines to derive their mean Doppler shifts and nonthermal widths. The results, listed in Table 6, have been derived according to the following procedure. First, we have computed the standard deviation of the heliospheric velocities measured for all the unblended lines of each ion. Then, we have selected the lines whose velocity is different from the mean by less than 1 standard deviation in order to remove from the analysis lines that might be altered by unknown blends or have inaccurate wavelengths. With these selected lines we then computed the mean heliospheric veloc-

Table 6 Doppler shift and nonthermal velocities of chromospheric and transition region lines measured in the STIS E140H spectrum of α Cen A

Ion	Log T_e	N^a	Velocity Shift ^b (km s ⁻¹)	Nonthermal Velocity (km s ⁻¹)	Notes ^c
Si I	3.80	80	0.00 ± 0.12	7.5 ± 0.3	
N I	3.85	5	-0.12 ± 0.10	14.6 ± 2.6	
S I	3.95	37	0.59 ± 0.07	7.6 ± 0.4	
C I	4.11	82	0.61 ± 0.09	9.9 ± 0.3	
Fe II	4.23	90	1.50 ± 0.17	10.8 ± 0.3	
Ni II	4.25	18	1.07 ± 0.34	10.9 ± 0.8	
Si II	4.26	9	1.21 ± 0.05	23.7 ± 2.3	
O I	4.31	3	1.01 ± 0.83	11.9 ± 3.2	
S II	4.48	2	2.27 ± 1.17	15.4 ± 0.4	
C II	4.62	2	1.68 ± 0.83	27.4 ± 1.3	1
C III	4.75	5	3.98 ± 0.64	28.7 ± 0.7	
Si III	4.78	3	6.92 ± 0.25	27.1 ± 1.3	
S III	4.81	1	5.05 ± 0.07	22.5 ± 0.3	1
Si IV	4.84	2	4.99 ± 1.47	25.7 ± 0.5	1
O III	4.97	2	4.73 ± 1.08	19.8 ± 7.3	1
C IV	5.03	2	7.28 ± 0.43	30.2 ± 1.0	1
O IV	5.21	2	7.25 ± 1.20	27.0 ± 0.5	
N V	5.25	2	3.87 ± 0.19	30.2 ± 1.1	1
S V	5.26	1	11.49 ± 0.93	38.9 ± 0.2	
O V	5.37	2	6.13 ± 1.25	33.1 ± 0.1	1

^aNumber of lines selected to compute the velocity shift and nonthermal velocity.

^bDoppler shift computed assuming as reference the measured mean velocity of Si lines, -23.85 ± 0.09 km s⁻¹.

^cWe use 1 in this column to flag the ions for which all the measured lines were used to compute the velocity shift and nonthermal velocity.

ity and standard deviation of the mean, as well as the mean FWHM. For some ions this procedure was not applied - e.g. in the case of ions for which less than 3 lines have been measured - as notated in the last column of Table 6.

The most probable nonthermal speeds (ξ) listed in Table 6 were computed from the measured FWHM (in km s⁻¹) by:

$$\left(\frac{FWHM}{c}\right)^2 = 3.08 \times 10^{-11} \left(\frac{2kT}{m_i} + \xi^2\right), \quad (1)$$

where c is the speed of light, T is the line formation temperature, and m_i the ion mass. The Doppler shifts listed in Table 6 are relative to the the mean velocity of the Si lines (-23.85 ± 0.09 km s⁻¹), which we use as the reference velocity, since the Si lines are formed deep in the chromosphere at a temperature close to 6500 K (Chae et al., 1998) and are expected to be at the rest velocity of the photosphere (Samain, 1991). This velocity is very close to the radial velocity of -23.45 km s⁻¹ obtained from contemporaneous AAT and CORALIE measurements (Pourbaix et al., 2002).

The Doppler shift and nonthermal widths of the chromospheric and transition region lines measured in the E140H spectrum of α Cen A are plotted in Figures 6 and 7. In both figures polynomial fits to the *SUMER* measurements of radial velocities and nonthermal widths in a solar active region and in the quiet Sun, derived by Teriaca et al. (1999), are represented with

dotted and dashed curves, respectively. According to Teriaca et al. (1999), in solar active regions the lines formed at temperatures between $T \sim 2 \times 10^4$ K and $\sim 5 \times 10^5$ K are red-shifted, with a maximum red-shift about 15 km s⁻¹ at $\sim 10^5$ K (C). At higher temperatures the velocities decrease becoming blue-shifted (about -10 km s⁻¹ at $T \sim 10^6$ K). However, in the quiet Sun the Doppler shift reaches a maximum at a slightly higher temperature, $T \sim 1.9 \times 10^5$ K (O , N), and then decreases to a blue-shift of about -2 km s⁻¹ at $T \sim 6.3 \times 10^5$ K (Ne).

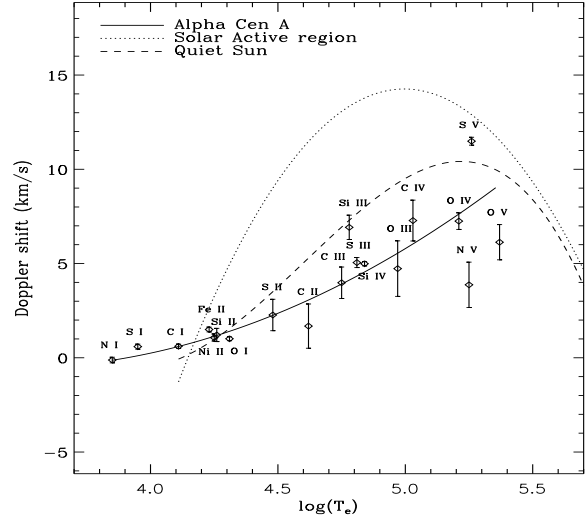


Fig. 6 Doppler shifts of chromospheric and transition region lines of α Cen A relative to the photospheric radial velocity as a function of the temperature of line formation. The solid line represents a fourth order polynomial fit to the data. The dotted and dashed lines are fits to the Doppler shifts for a solar active region and the quiet Sun, respectively, by Teriaca et al. (1999).

We performed a 2nd order polynomial fit to the α Cen A line Doppler shifts with respect to the temperature of line formation, giving each data point a weight equal to the square root of the inverse of its standard deviation. We find that in the sampled temperature range ($T \sim 7 \times 10^3$ K to $T \sim 2.3 \times 10^5$ K) the redshift increases monotonically, but the data are not adequate to infer the temperature of the turnover. Even though the lines of C , Si , and Fe are believed to be optically thick, these lines do not show Doppler shifts different from the optically thin lines formed at the same formation temperature. The N lines, especially the 1238 Å line, have broad wings, and their centroids show a smaller redshift than is expected by the general distribution. In fact, the broad components are generally marginally blueshifted relative to the narrow components, as discussed in Section 3.3.

For both active and quiet regions on the Sun, the distributions of nonthermal line width versus line formation temperature, derived by including only those lines that are not affected by opacity effects, show a peak at $T \sim 5 \times 10^5$ K. To map the increase in turbulent velocity with line formation temperature (and hence approximate height in the atmosphere), we fit the α Cen A data with a third order polynomial using the widths of the optically thin lines. In the sampled temperature interval,

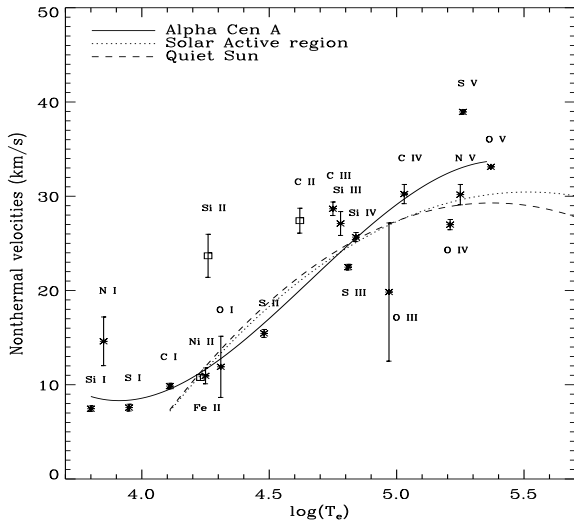


Fig. 7 Nonthermal velocities of chromospheric and transition region lines as function of the temperature of line formation. The solid line represents a third order polynomial fit to the data. Lines which are possibly affected by opacity (Fe, Si, and C) are not included in the polynomial fit (*square data points*). The dotted and dashed lines represent the nonthermal line widths in a solar active region and in the quiet Sun, respectively, as derived by Teriaca et al. (1999).

the turbulent velocity distribution for α Cen A resembles the solar data, although slightly larger nonthermal line widths are measured for line formation temperatures greater than $T \sim 10^5$ K. We note that the O mean line width is probably underestimated because the 1660 Å line may be blended, which can alter its intensity and consequently the determination of its width.

5. Comparison between the UV spectra of α Cen A and the Sun

5.1. The Solar UVSP/SMM and SUMER/SOHO spectra

Solar UV spectra with comparable spectral resolution to our HST/STIS spectrum of α Cen A are those observed by the UltraViolet Spectrometer and Polarimeter (UVSP) instrument which flew on the the Solar Maximum Mission (SMM) and by the SUMER (Solar Ultraviolet Measurements of Emitted Radiation) spectrograph now operating on SOHO (Solar and Heliospheric Observatory).

The UVSP/SMM spectrum was obtained during the minimum of solar cycle (1984) in the range 1290 – 1772 Å with a $1'' \times 180''$ slit, oriented north-south near solar disk center, with spectral resolution of the order of 100,000. The atlas (2nd order) was prepared by Richard Shine and Zoe Frank of the Lockheed-Martin Space and Astrophysics Lab., and was retrieved from the site ftp://umbra.nascom.nasa.gov/pub/uv_atlases/. According to Shine (private communication), this spectrum was calibrated using Rottman’s quiet Sun data from rocket flights, which had accurate flux scales but had low spectral resolution. For inter-comparison purposes, the wavelength scale of the solar spectrum was shifted by performing a cross correlation between this

spectrum and the α Cen A spectrum in many selected wavelength intervals.

The SUMER/SOHO spectrum is the FUV part of the spectrum that has been derived from observations obtained in the range 670 – 1609 Å by Curdt et al. (2001). These data were acquired with a dispersion of ~ 41.2 mÅ/pixel (1st order) at 1500 Å, for an effective resolution of ~ 8.2 km s $^{-1}$. The wavelengths are typically accurate to 10 mÅ, i.e. 2 to 5 km s $^{-1}$. The data represent the average radiance (mW sr $^{-1}$ m $^{-2}$ Å $^{-1}$) for the quiet Sun at disk center (April 20, 1997), a coronal hole (Oct 12, 1996), and a solar spot (Mar 18, 1999). Hence, the quiet Sun and coronal hole SUMER spectra were acquired during phases of minimum of the solar cycle.

To be comparable with the α Cen A spectrum, we have computed the solar irradiance at the α Cen distance from the quiet Sun radiance at disk center by multiplying by $\pi R_{\odot}^2/d_{\alpha Cen}^2$ (cf. Wilhelm et al. 1998) for the quiet Sun, sunspot, and coronal hole spectra. This conversion does not take into account center-to-limb variations in the lines and continuum.

5.2. Comparison between the α Cen A/STIS and the Sun/UVSP spectra

The comparison between the STIS α Cen A and the UVSP solar spectra can be made in the 1192–1688 Å spectral range. In Figure 4 we plot interesting regions of the UVSP spectrum and the α Cen A spectrum degraded to a resolution of 0.010 Å/pixel in order to be comparable to the UVSP spectrum. The wavelength scale of the α Cen A spectrum was shifted to compensate for the radial velocity of the system (-23.45 km s $^{-1}$).

Since the UVSP data refer to the “mean intensity over the disk”, it is possible to perform a radiometric comparison with the α Cen A spectrum. For the emission lines whose integrated flux in the STIS spectrum exceed 5×10^{-14} erg s $^{-1}$ cm $^{-2}$, we list in Table 7 line surface fluxes and full widths at half maximum (FWHM) for both α Cen A and the Sun. We find that the line widths for the two stars are very similar for most of the chromospheric lines, whereas the transition region lines are typically broader for α Cen A compared to the Sun. We show in Figure 8 the FWHM ratios versus the temperatures of line formation. A linear fit to these data suggests that the two quantities are correlated with a correlation coefficient of 0.83. Typically the α Cen A line surface fluxes are slightly larger than those of the Sun (see Figure 9), with a mean flux ratio (Sun/ α Cen A) of 0.83 ± 0.18 , but the Si 1526 and 1533 Å, the He 1640 Å and the Al 1671 Å lines are stronger in the Sun than in α Cen A. The interstellar medium absorption in the Si 1526 Å and Al lines of α Cen A can partially explain the high flux ratios. However, this is not the case for the Si 1533 Å line. The common factor for the three lines is the presence of central reversals. In the Sun these lines form in the chromosphere, where temperature increases with height. Line source functions, however, first increase and then decrease with height over the line formation region, due to non-LTE effects. A central reversal occurs for an optically thick line when the line core forms above the region where the source function peaks. The “horns” of the observed profile form roughly where the source function peaks

Table 7 Surface fluxes (in units of $10^3 \text{ erg cm}^{-2} \text{ s}^{-1}$), and FWHM (km s^{-1}) of a selection of lines present in the spectra of both α Cen A and the Sun. Included lines have fluxes in the α Cen A spectrum greater than $5 \times 10^{-14} \text{ erg s}^{-1} \text{ cm}^{-2}$.

Line ID	Lab Wavel. (Å)	Surface Flux		Flux Ratio	FWHM		FWHM Ratio	Line ID	Lab Wavel. (Å)	Surface Flux		Flux Ratio	FWHM		FWHM Ratio
		α Cen A	Sun	$\frac{\text{Sun}}{\alpha \text{ Cen A}}$	α Cen A	Sun	$\frac{\text{Sun}}{\alpha \text{ Cen A}}$			α Cen A	Sun	$\frac{\text{Sun}}{\alpha \text{ Cen A}}$	α Cen A	Sun	$\frac{\text{Sun}}{\alpha \text{ Cen A}}$
S I	1300.907	0.15	0.12	0.82	13	18	1.36	C I+	1608.438	0.30	0.46	1.55	31	28	0.92
O I	1302.169	1.98	1.80	0.91	33	32	0.96	+Fe II							
Si II	1304.372	0.18	0.16	0.88	31	33	1.04	Fe II	1610.921	0.31	0.24	0.76	23	20	0.89
O I	1304.858	2.10	1.84	0.88	33	27	0.80	Fe II	1611.201	0.21	0.17	0.82	17	15	0.85
O I	1306.029	2.17	1.96	0.90	29	24	0.83	Fe II	1612.802	0.39	0.34	0.87	26	26	0.97
C II	1334.532	3.27	2.68	0.82	43	31	0.74	C I	1613.376	0.18	0.15	0.85	12	13	1.12
C II	1335.708	4.53	3.82	0.84	47	36	0.76	C I	1613.803	0.17	0.13	0.77	12	13	1.07
Cl I	1351.657	0.30	0.32	1.06	12	12	0.97	C I	1614.507	0.19	0.13	0.68	13	12	0.97
O I	1355.598	0.46	0.42	0.91	12	12	0.99	Fe II	1618.470	0.25	0.30	1.21	24	20	0.83
Si IV	1393.755	2.22	2.14	0.97	44	31	0.72	Fe II	1623.091	0.28	0.25	0.89	24	22	0.92
O IV]	1401.157	0.23	0.16	0.72	46	36	0.79	Fe II	1625.520	0.47	0.32	0.69	27	23	0.86
Si IV	1402.770	1.12	0.83	0.75	42	29	0.69	Fe II	1625.909	0.20	0.20	0.98	17	18	1.02
O IV]+	1404.806	0.12	0.08	0.66	47	45	0.97	Fe II	1632.668	0.37	0.39	1.06	20	18	0.90
+S IV								Fe II	1633.908	0.37	0.32	0.86	26	24	0.94
S I	1472.972	0.38	0.28	0.74	18	18	1.02	Fe II	1637.397	0.49	0.43	0.89	25	24	0.94
S I	1473.995	0.21	0.20	0.92	16	15	0.96	Fe II	1640.152	0.52	0.69	1.33	22	22	1.00
N IV	1486.496	0.16	0.06	0.40	45	33	0.74	He II	1640.400	0.62	1.60	2.59	52	52	1.00
Si II	1526.708	0.67	1.64	2.44	32	32	0.98	Fe II	1643.576	0.45	0.42	0.94	22	22	1.00
Si II	1533.432	0.74	1.65	2.23	37	31	0.86	Fe II	1649.423	0.30	0.21	0.71	22	18	0.84
C IV	1548.187	4.50	5.11	1.13	49	45	0.88	C I	1656.260	1.68	2.05	1.22	37	30	0.84
Fe II	1550.260	0.13	0.11	0.89	20	20	1.01	C I	1656.928	1.34	2.25	1.69	58	54	0.92
C IV	1550.772	2.39	2.39	1.00	52	47	0.88	C I	1657.380	1.51	1.86	1.23	35	31	0.89
Fe II	1559.084	0.47	0.39	0.82	30	29	0.96	C I	1657.900	0.99	1.52	1.53	28	27	0.96
C I	1560.310	0.51	0.60	1.17	27	29	1.06	C I	1658.120	1.22	1.76	1.44	30	26	0.87
C I	1560.683	0.60	0.73	1.22	30	36	1.21	Fe II	1658.771	0.50	0.42	0.83	24	20	0.85
C I	1561.341	0.83	1.19	1.42	56	51	0.92	Fe II	1659.483	0.75	0.69	0.91	27	26	0.97
Fe II	1563.788	0.42	0.37	0.88	28	26	0.92	O III	1660.803	0.17	0.12	0.73	20	22	1.07
Fe II	1566.819	0.30	0.25	0.81	25	24	0.96	O III	1666.153	0.31	0.13	0.43	45	34	0.76
Fe II	1569.674	0.24	0.29	1.24	22	22	0.99	Fe II	1669.663	0.22	0.15	0.67	16	12	0.75
Fe II	1570.242	0.35	0.39	1.12	23	25	1.07	Al II	1670.787	1.78	3.57	2.01	44	41	0.94
Fe II	1577.166	0.15	0.19	1.22	18	18	0.95	Fe II	1674.254	0.40	0.35	0.87	20	17	0.85
Fe II	1580.625	0.30	0.30	1.02	22	24	1.07	Fe II+	1685.954	0.29	0.38	1.30	23	21	0.92
Fe II	1584.949	0.28	0.30	1.08	23	22	0.94	+Ni II							
Fe II	1588.286	0.36	0.55	1.53	21	19	0.90	Fe II	1686.455	0.44	0.55	1.26	23	20	0.84
C I	1602.972	0.13	0.13	0.99	15	16	1.07	Fe II	1686.692	0.60	0.59	0.99	25	26	1.04

(Mauas et al., 1989). On the Sun we see that the depth of the central reversal is a function of position on the solar surface. For example, the C lines of the multiplet at 1560 and 1657 Å show profiles which have central reversals quite deep at the limb, and less pronounced both above the limb and towards disk center (Roussel-Dupré, 1983). The UVSP spectrum was acquired near disk center, while the α Cen A spectrum is a full disk average. As a consequence, we expect less pronounced central reversals for the strongest chromospheric lines in the solar UVSP spectrum than in the α Cen A spectrum, as is observed.

We believe that the He line, which is optically thin and not self-reversed, is really weaker on α Cen A than on the Sun. Since the He line is extremely sensitive to the coronal activity, a flux ratio of 1.8 suggests that the Sun is more active than α Cen A. This conclusion is strengthened by the absence of a limb contribution in the solar data since the He line is limb-brightened for the Sun and likely also for α Cen A.

It should be mentioned here that some of the UV line flux differences between the α Cen A and the Sun may be due to observing at different phases of the two stellar activity cycles. In fact transition region lines on the Sun can vary up to factors 2 – 5 over a magnetic cycle. While both UVSP and SUMER spectra were acquired during phases of solar minimum, we do not know the phase of α Cen A activity cycle at which our observations have been obtained. In fact, the long-time extended IUE data base of α Cen A does not provide any hints of an activity cycle period (Ayres et al., 1995). The roughly 13 individual measurements of the C IV multiplet flux obtained by IUE over a 13 year time period (see Fig. 11a in their paper) have a mean value of $(2.500 \pm 0.071) \times 10^{-12}$ but a range from 1.5 to 3.6 in these units. The STIS flux for the C IV multiplet is 2.80 in the same units. This STIS flux is about 12% larger than the mean IUE flux. Since the IUE data are low resolution (about 6 Å), the broad line wings could be difficult to measure compared to the continuum and nearby weak lines. Thus the C IV fluxes

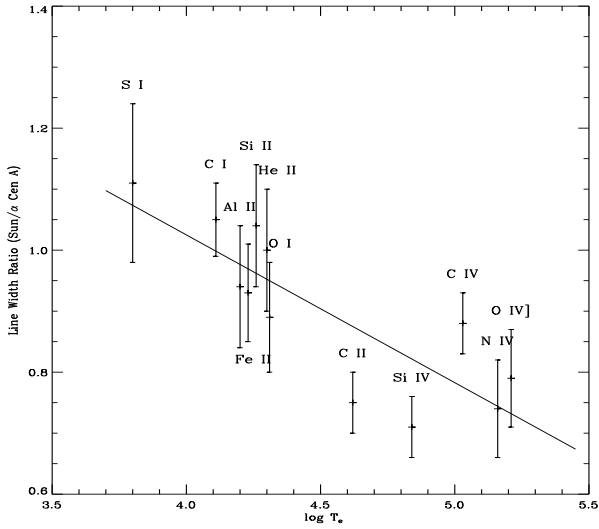


Fig. 8 Ratios of the solar to α Cen A line widths versus the temperatures of line formation.

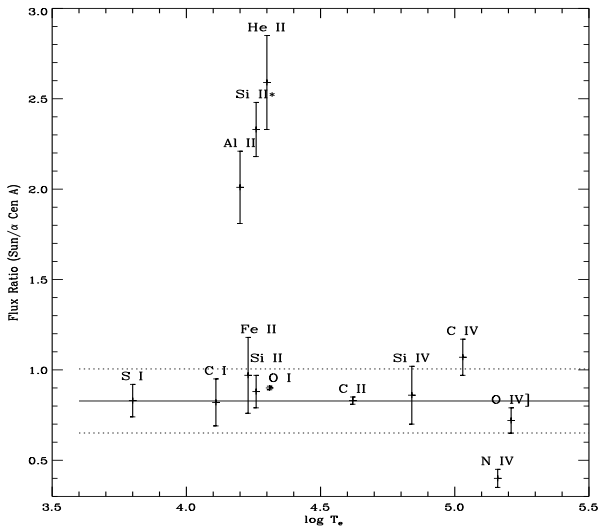


Fig. 9 Ratios of the solar to α Cen A line surface fluxes versus the temperatures of line formation. The * label identifies the Si lines at 1526 and 1533 Å.

measured from IUE spectra are likely somewhat low, and the C IV flux observed by STIS is probably very close to the mean value observed by IUE. We therefore believe that α Cen A had average transition region fluxes when it was observed by STIS.

5.3. Comparison between the α Cen A/STIS and Sun/SUMER spectra

In Figure 10 we plot interesting regions of the α Cen A spectrum, and the SUMER spectra of a coronal hole, a sunspot, and the quiet Sun, respectively. The wavelength scale of the α Cen A spectrum was shifted to remove the radial velocity of the star (-23.45 km s^{-1}). The SUMER spectrum has the best photon statistics, therefore faint lines can be more easily seen in the solar spectrum than in the α Cen STIS spectrum. On the other hand, the STIS spectrum has better resolution, which can

Table 8 Measured features in the 1170-1610 Å common spectral range.

	Total Features	With ID ^a	Without ID ^a
α Cen A/STIS	559	498	61
- of which not in the solar spectrum	172	127	45
Sun/SUMER	516	458	58
- of which not in the α Cen A spectrum	126	80	46
Lines common to both spectra	390	377	13

^a ID = Identification

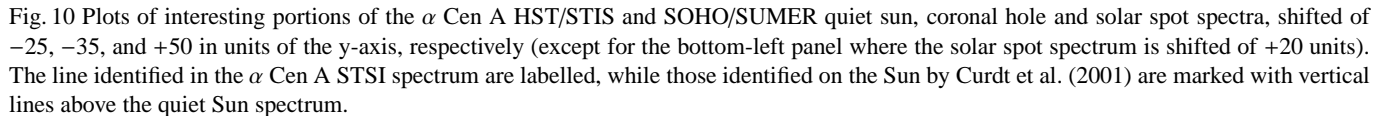
be useful in resolving line blends and in studying line reversals due to optical thickness effects better than with the solar spectrum. In Table 8 we summarize how many lines we found in common between the two spectra. Many of the lines present in the solar spectrum but not in α Cen A are located at wavelengths below about 1500 Å, whereas many of the lines detected only in the STIS spectrum are at wavelengths above 1500 Å. These differences probably result from the different resolutions of the two data sets and the increasing S/N of the SUMER data to shorter wavelengths. The emission lines in the α Cen A spectrum are much stronger than in the quiet Sun spectrum. This is most likely because we are comparing the solar spectrum, which is an average disk-center quiet Sun spectrum, with the α Cen A full disk irradiance spectrum, which includes emission from the limb. For most of the lines, the full disk irradiance is nearly a factor of two larger than the irradiance derived from disk-center radiance data (cf., Wilhelm et al. 1999), but there is no difference for the continuum. Because of this effect, the radiometric comparison between the SUMER and STIS spectra is uncertain.

6. Electron Densities

The ratios of lines emitted by the same ion can be sensitive to electron density when the upper levels of the two transitions are depopulated in different ways. However, misleading results can be obtained when using line ratios that have a very small sensitivity at the inferred electron densities or when temperature effects are not properly taken into account. For this reason we have computed transition region densities for α Cen A using both the line ratios method and the so-called L-functions method, as described by Landi & Landini (1997). The main advantage of this method is that it gives an overall view of all lines and clearly shows which lines (and not line ratios) are more suitable in a particular density regime and when lines are at the limit of their density sensitive regime. According to these authors, the *contribution function* for each line of a selected ion, $G_{ij}(T, N_e)$, can be expressed as a product of two functions, one depending on electron density and electron temperature, and the other on temperature alone:

$$G_{ij}(T, N_e) = f_{ij}(N_e, T)g(T). \quad (2)$$

While the $g(T)$ function is mainly determined by the ionization equilibrium and is the same for all the lines of the same ion, $f(N_e, T)$ is determined mainly by the population of the upper



The analysis of the α Cen A electron densities have been carried out with the help of the CHIANTI database VERSION 4.0 (Dere et al. 1997; Young et al. 2003), assuming the ionization equilibria described by Mazzotta et al. (1998) and the α Cen A photospheric abundances listed in Table 2.

The O I intercombination multiplet near 1400 Å can be used as a density diagnostic in the range $10^9 < N_e < 10^{12} \text{ cm}^{-3}$ (Brage et al., 1996). The 5 lines of the multiplet are all measured in the α Cen A STIS spectrum. The 1399.780 and 1407.382 Å lines originate from a common upper level; their ratio is 1.00 ± 0.26 , consistent with the ratio of their A-values (1.08), which is the expected value for a branching ratio in the optical thin case (Jordan, 1967). The O I 1404.806 Å line is blended with S I 1404.808 Å, and possibly with another unknown line (Del Zanna, Landini, & Mason, 2002). The percentage of the blend-

In Figure 11 (*top panel*) the L-functions of the O lines, computed at $T_{eff} = 5.18$, are plotted versus $\log N_e$. Apart from the 1397 Å line, which is very weak and results in large errors, the other lines meet at $\log N_e \sim 10.0$, assuming that the O 1404 Å line accounts for 70% of the blend.

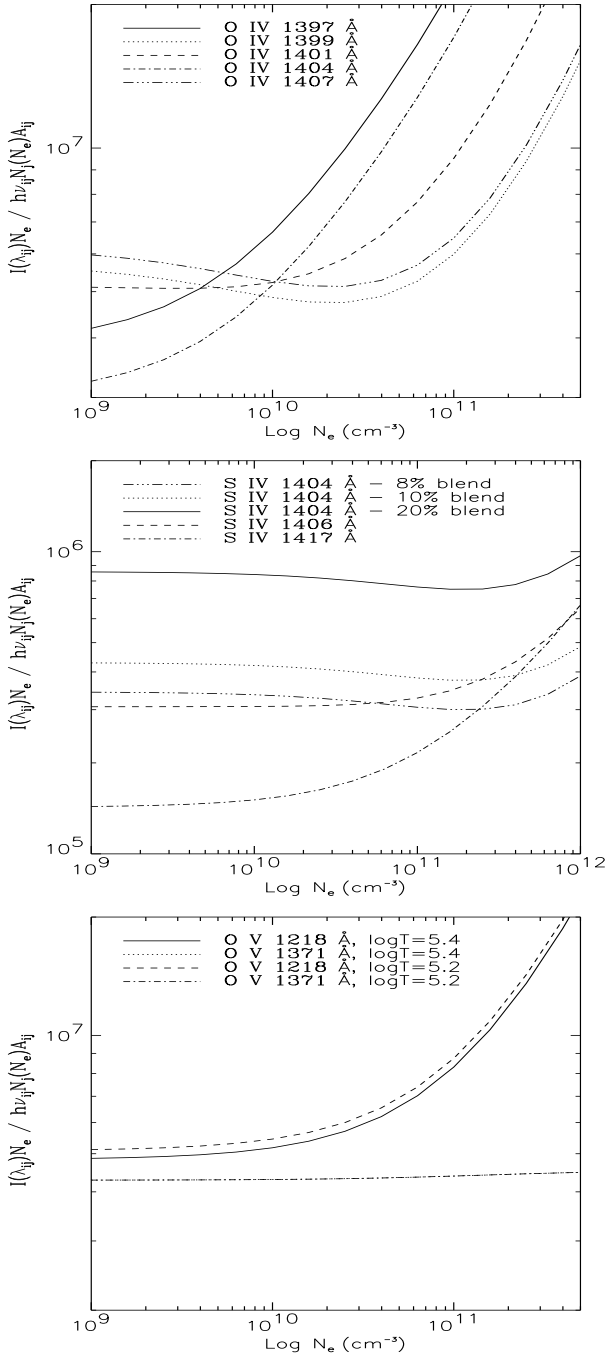


Fig. 11 The L-function curves (as defined by Landi & Landini 1998) plotted for the O λ , S λ , and O λ 1218 and 1371 Å lines observed in the STIS spectrum of α Cen A.

The L-functions of the S λ 1404, 1406, and 1407 Å lines, plotted in Figure 11 (*middle panel*), show that in order to have consistency among the lines, the S λ 1404 Å line must not exceed 10% of the flux in the blend. Therefore, an unidentified line contributes ~ 10 –20% of the total flux to the 1404 Å blend. Moreover, the L-functions of the S λ lines clearly show that no reliable density measurements can be derived from these lines.

6.2. O v

The observed O λ 1218/1371 Å line ratio is $R = 12.41 \pm 2.50$. Using the Chianti code, and assuming the ionization equilibrium as described in Mazzotta et al. (1998) and the α Cen A photospheric abundances listed in Table 2, we find that:

- at the O λ effective temperature, $\log T_e = 5.53$, the theoretical 1218/1371 line ratio varies in the range $\sim [1, 6]$, corresponding to $\log N_e \sim [12, 10]$;
- at the temperature of O λ maximum ionization fraction, $\log T_e = 5.40$, the theoretical line ratios fall in the range $\sim [1, 7]$, corresponding to $\log N_e \sim [12, 9.5]$.

Therefore, the observed ratio 12.41 ± 2.50 is not consistent with the theoretical ratios for any sensible density. In fact, the L-functions of the O λ 1218 and 1371 Å lines shown in Figure 11 (*bottom panel*) at temperature $\log T_e = 5.4$ do not cross at any density.

Either an overestimation of the 1218 Å O λ line flux or an underestimation of the 1371 Å line flux can produce this higher than expected flux ratio. The 1218 Å line would have to be less than half the measured value, or the 1371 Å line would have to be more than double the measured value, to be consistent with a density $\log N_e > 10$ at $\log T_e = 5.4$. As discussed in Section 3.2 and shown in Figure 2, the O λ line at 1371 Å appears in the STIS spectrum with a double peak, indicating an apparent central reversal or overlying absorption. We know of no explanation for this effect, but it could be the cause of a slight flux underestimation for this line. On the other hand, in Section 7 we show that the density sensitive O λ 1218 Å line does not match the differential emission measure distribution determined from the allowed lines at any density, unless we assume that its actual flux is from 20 to 30% less than measured. We think that such an error can be ascribed to the difficulty in measuring the O λ line in the sloping wing of the Ly α line, as already discussed in Section 3.2, where we also show a slight discrepancy in the radial velocities measured for the O λ 1218 and 1371 Å lines.

7. The α Cen A emission measure distribution

The physical properties of the transition region plasma can be determined by means of an emission measure distribution analysis (cf. Jordan & Brown 1981; Dere & Mason 1981; Pagano et al. 2000). The frequency integrated flux F_{ji} of an effectively thin emission line between levels j and i of an atom, in units $\text{erg cm}^{-2} \text{s}^{-1}$, can be written as:

$$F_{ji} = \frac{h\nu_{ji}}{2} \int_{\Delta z} \frac{N_j A_{ji}}{N_e^2} N_e^2 dz, \quad (3)$$

where N_j (cm^{-3}) is the number density of the upper level, A_{ji} (s^{-1}) is the Einstein A-coefficient of the line for a transition between levels j and i , and N_e (cm^{-3}) is the electron density. With a high degree of accuracy, the ratio $\frac{N_j A_{ji}}{N_e^2}$ is a function only of temperature T_e and density N_e . For resonance lines formed at transition region temperatures, this ratio is a weak function of

N_e and a strongly peaked function of T_e , say $f(T_e)$. Therefore, defining the *differential emission measure* $\xi(T_e)$ as:

$$\xi(T_e) = N_e^2 \frac{dz}{d\log_{10} T_e}, \quad (4)$$

equation 3 can be written as:

$$F_{ji} = \frac{h\nu_{ji}}{2} \int_{\Delta\log_{10} T_e} f(T_e) \xi(T_e) d\log_{10} T_e. \quad (5)$$

The differential emission measure $\xi(T_e)$ can in principle be determined from a set of emission line fluxes, by an inversion of the set of the corresponding integral equations (eq. 5). The total emission measure for the emitting plasma is the integral over $\log T_e$ of the $\xi(T_e)$ function. Since emission lines are typically formed over a temperature range of $\Delta\log T_e \sim 0.3$, we determine the differential emission measure $\xi^{0.3}(\log T_e)$ for all plasma with temperature in the range $\log T_e - 0.15$ to $\log T_e + 0.15$. The shape of the emission measure distribution is constrained by the combination of the loci from different emission lines, where the *emission measure locus* of each line, in units of cm^{-5} , is given by:

$$E_m^{ji}(\log T_e) = \int_{\Delta z} N_e^2 dz = \frac{F_{ji}}{\frac{h\nu_{ji}}{2} f(\log T_e)} = \frac{F_{ji}}{G_{ji}(\log T_e)}, \quad (6)$$

where $E_m^{ji}(\log T_e)$ represents the amount of isothermal material needed to produce the observed line flux.

We have derived the emission measure loci as a function of temperature for each emission line of interest using equation 6, the $G_{ji}(\log T_e)$ functions computed with the CHIANTI database VERSION 4.0 (Dere et al. 1997; Young et al. 2003), the ionization equilibrium as in Mazzotta et al. (1998), and the α Cen A photospheric abundances listed in Table 2. Following the procedure described in Pagano et al. (2000), we derive the differential emission measure distribution shown in Figure 12. We used the allowed lines of Si, S, C, S, Si, C, S, O, and Fe observed in the STIS spectrum, which are labelled in the last column of Table 3 with the letters “emd”. We have also used the allowed lines C 1036 & 1037 Å, N 990 Å, S 1077 Å, Si 1108 Å, S 1062 & 1063 Å, Ne 1145 Å, and O 1037 Å observed in the FUSE spectrum of α Cen A (Redfield et al., 2002). When more than two lines for a given ion have been used, the errorbars in Figure 12 represent the standard deviation of the emission measures computed for the different lines. Otherwise, the errorbar is indicative of the uncertainty due to the line flux measurement. The allowed C 1548 & 1502 Å, Si 1393 & 1402 Å, N 1238 & 1242 Å, and S 933 Å lines were not used to derive the differential emission measure distribution, because Del Zanna, Landini, & Mason (2002) showed that such lines from the Li and Na isoelectronic sequences, which were commonly used in previous literature, produce erroneous results in the determination of emission measures. In Figure 12 emission measure loci of the C, Si, N, and S lines are, in fact, anomalous with respect to the emission measure distribution derived from the other ions.

In Figure 12 we also plot for comparison the differential emission measure distribution for the quiet Sun (Landi &

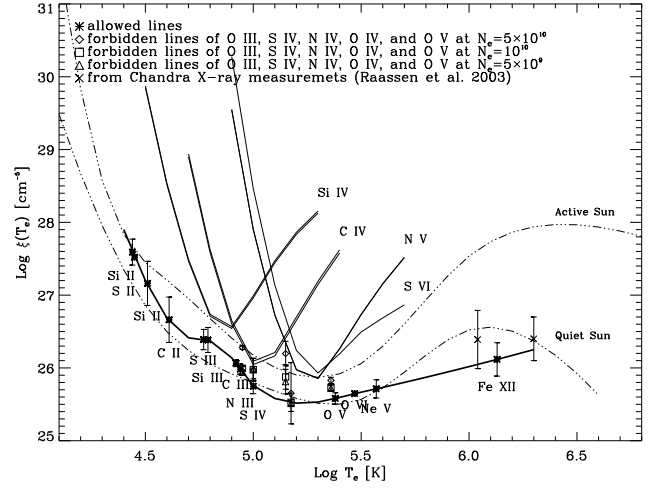


Fig. 12 The differential emission measure distribution of α Cen A (solid thick line) is compared with corresponding distributions for the quiet Sun and active Sun. The intersystem lines of O 1666 Å, and of the O IV UV 0.01 multiplet near 1400 Å match the differential emission measure distribution for electron density of $\log N_e = 9.5-10$ [cm^{-3}]. The Chandra X-ray data are from Raassen et al. (2003).

Landini, 1998) and for solar active regions (Dere & Mason, 1993). There is close agreement between the differential emission measure distributions of α Cen A and the quiet Sun in the $\log T$ range 5.0–5.6. For temperatures below $\log T \sim 5.0$, the emission measure is larger for α Cen A than for the quiet Sun. At temperatures higher than $\log T \sim 5.6$ we have only the Fe 1242 Å line in the STIS spectrum, therefore it is not possible to constrain the real slope of the emission measure distribution. There is, however, a reasonable good agreement between the emission measure of Fe and the values derived at temperatures $\log T = 6.04$ and 6.3 from Chandra spectra (Raassen et al., 2003).

The spin-forbidden lines can be used to obtain information on the plasma density by comparing their emission measure loci, computed for different values of the density, with the emission measure distribution derived by using the resonance lines. In fact, for collisionally de-excited spin-forbidden lines (i.e., when $N_e C_j > A_{ji}$ and $C_j = \sum_i C_{ji} \text{ cm}^{-3} \text{ s}^{-1}$ is the total collision rate out of level j), the ratio $N_j A_{ji} / N_e^2$ in Equation 3 is proportional to $f(T_e) / N_e$. Therefore, the emission measure loci of spin-forbidden lines depend upon both electron density and temperature. In Figure 12 we have plotted the emission measures of the intersystem O 1666 Å, S 1406 Å, N 1486 Å, and O 1218 Å lines, and the mean emission measure of the O lines at 1397, 1399, 1401, and 1407 Å. The O and O ions match the emission measure distribution derived from allowed lines for electron density $\log N_e = 9.5-10$, and lie above at higher densities. The S, N, and O lines do not strictly match the emission measure distribution at any density. A possible explanation for this behaviour is that the fluxes of these lines are slightly overestimated (no more than 50%). As shown in Figure 13, the S 1406 Å and N 1486 Å lines are very well detected in the STIS α Cen A spectrum, and a flux overestimation could be caused only by unknown

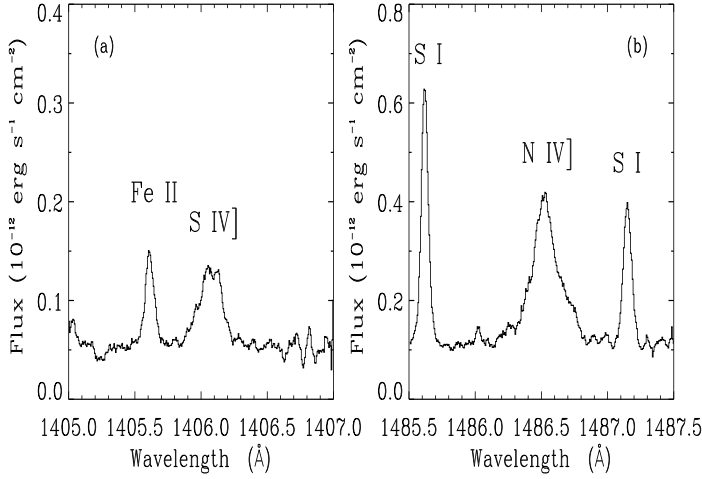


Fig. 13 The S IV] 1406 Å line (panel a) and the N IV] 1486 Å line (panel b) discussed in Section 7.

blends. Alternatively, inaccurate atomic data could be the cause of the observed discrepancy. For the O 1218 Å line, a flux from 20 to 30% less than measured would make this line consistent with the emission measure distribution derived from the allowed lines. As seen in Section 6.2, the anomalous ratio between 1218 and 1371 Å line fluxes also suggests that the O 1218 Å line flux was overestimated, possibly because of the sloping Ly α wings (cf. Section 3.2).

The total power radiated per unit (surface) area from the stellar atmosphere is:

$$P = \int_{T_{\min}}^{T_{\max}} \frac{N_H}{N_e} P_{\text{rad}}(T_e) \frac{\xi(T_e)}{T_e} dT_e, \quad (7)$$

where P_{rad} is the total power radiated in all spectral features per unit emission measure and for a specified set of atomic abundances. Above $\log T_e \sim 4.0$ hydrogen is predominantly ionized, therefore $N_H/N_e \sim 0.8$. By using the analytical expression for P_{rad} given by Rosner et al. (1978) and the differential emission measure derived above, we find a radiative power loss of $1.5 \times 10^6 \text{ erg s}^{-1} \text{ cm}^{-2}$, i.e. $2.4 \times 10^{-5} L_{\text{bol}}$, for the plasma in the temperature range $\log T_e = 4.4 - 6.5$. This result is compatible with the estimate of the total power radiated between 10^4 and 10^8 K, excluding hydrogen emission, which can be computed from the surface flux of the C lines by using the Bruner & McWhirter (1988) empirical relation, $P = f(\text{CIV } 1548 + 1550 \text{ Å}) / 3.0 \times 10^{-4}$. For α Cen A this formula predicts $P = 5.7 \times 10^{-5} L_{\text{bol}}$. Focusing on only the regions for which we have derived a very well constrained emission measure distribution, that are those in the temperature range $\log T_e = 4.4 - 5.6$, we find that their radiative power loss is $4.2 \times 10^5 \text{ erg s}^{-1} \text{ cm}^{-2}$ or $6.5 \times 10^{-6} L_{\text{bol}}$.

With the same method described above, we have computed the power loss from Solar Active regions and from the Quiet Sun adopting their emission measure distributions as in Figure 12. For the temperature range $\log T_e = 4.4 - 5.6$ we find a power loss of $8.3 \times 10^5 \text{ erg s}^{-1} \text{ cm}^{-2}$ ($1.3 \times 10^{-5} L_{\text{bol}}$) from Solar Active Regions, and of $2.6 \times 10^5 \text{ erg s}^{-1} \text{ cm}^{-2}$ ($4.0 \times 10^{-6} L_{\text{bol}}$) from the Quiet Sun. The α Cen A power loss in the same temperature range is therefore midway between those

of the Quiet Sun and the Solar Active Regions, but closer to the former than to the latter.

8. The Interstellar medium towards α Cen

A number of lines in the α Cen A spectrum contain interstellar absorption components (look for label "ISM" in the *Notes* column of the Table 3). The analysis of these components will be presented and analyzed in a subsequent paper. We call here attention to the narrow absorption features in the Si 1393 Å, C 1548 Å, and N 1238 Å lines shown in Figure 5. We think that these features could be real. In fact, if they were an artifact of the line spread function, then they would appear in all emission lines, not just the high excitation lines. Also the possibility that these features are the results of order overlapping, in the case the wavelength scales of two adjacent orders were not consistent, was examined and disregarded. In fact, not one of the above emission lines lies in the overlap region of two adjacent orders. Although the central reversals in N and perhaps C could be noise, the reversal in the Si line appears to be too deep and includes too many pixels to be just noise. The reality of the Si IV feature suggests that the other features could be real. If the reversals are real, then what is their cause? Self-absorption should affect both lines in a doublet, but the weaker members of the doublet do not show absorption features. Perhaps we are detecting narrow absorption by some cool species above the hot regions. Since these possible absorption features are too narrow to be thermal, we have no explanation for them, and further observations and analysis are needed to verify their reality and, if real, search for their cause.

9. Conclusions

We present our analysis of HST/STIS observations of α Cen A and compare its spectrum with its near twin, the Sun:

(1) We present a high resolution ($\lambda/\Delta\lambda = 114,000$) spectrum of α Cen A obtained using the E140H mode of STIS that covers the spectral range 1140–1670 Å with very high signal-to-noise. The spectrum has an absolute flux calibration accurate to $\pm 5\%$, an absolute wavelength accuracy of 0.6–1.3 km s $^{-1}$, and is corrected for scattered light. To our knowledge this is the best available ultraviolet spectrum of a solar-like star.

(2) As strange as this may at first appear, there is no available ultraviolet reference spectrum of the Sun as a point source with the characteristics of the α Cen A spectrum that can be used to compare stellar spectra with the Sun. Many ultraviolet spectra of the Sun do exist, but they either have lower spectral resolution, lack wavelength or flux accuracy, or do not include the center-to-limb variation across the solar disk required to provide an accurate spectrum of the Sun as a point source. Although α Cen A differs slightly from the Sun in effective temperature, gravity, and metal abundance, its spectrum can serve as a representative solar spectrum for comparison with other stars.

(3) We compare the α Cen A spectrum to the solar irradiance (the Sun viewed as a point source) derived from UVSP data for the "mean intensity over the disk" by placing the Sun at the distance to α Cen A and shifting the α Cen A spectrum

by the star's radial velocity. The line widths of the two stars are similar for chromospheric lines, but the transition region lines of α Cen A are broader than those of the Sun by roughly 20%. The line surface fluxes are typically larger on α Cen A, presumably due to α Cen A being somewhat metal rich. However, the He 1640 Å line is stronger in the Sun, indicating that the solar corona is more active.

(4) We also compare the α Cen A spectrum to the solar irradiance derived from SUMER spectra of the disk center quiet Sun, assuming constant center-to-limb radiance and shifting the α Cen A wavelength scale by the radial velocity of the star. A total of 671 emission lines are detected in the α Cen A spectrum from 37 different ions and 2 molecules (CO and H₂). In addition to the well known chromospheric and transition region lines, we also identify lines of Al, Si, S, Ca, Fe, Fe, and Fe. A total of 172 emission lines observed in α Cen A are not seen in the SUMER spectrum.

(5) Broad wings are present in the strong resonance lines of C, N, Si, and Si, as are seen in solar observations of the chromospheric network. We fit the line profiles with two Gaussians: a narrow component ascribed to Alfvén waves in small magnetic loops, and a broad component ascribed to microflares or magneto-acoustic waves in large coronal funnels. Both components are redshifted with the narrow Gaussians having larger redshifts as is seen on the Sun. At line formation temperatures between 20,000 K and 200,000 K, there is a trend of increasing line redshift, similar to but with a somewhat lower magnitude than the quiet Sun. A similar trend of increasing nonthermal velocities with temperature is nearly identical to that which is observed in solar quiet and active regions.

(6) Using line ratios and L-functions, we infer that the O lines are formed where the electron density is $\log N_e \sim 10.0$. The S and O lines, however, do not provide reliable N_e values. Values of N_e have been obtained for the Sun and other solar type stars (c.f. Cook et al. 1995). It is hard to make any comparison with these results because they are strongly affected by the adopted atomic calculation or by the choice of lines with a limited density sensitivity, as the O 1400 Å line (see Del Zanna, Landini, & Mason 2002). Hence estimates of N_e from different computations are often not consistent. We can, however, compare the electron density we derive for α Cen A at $\log T \sim 5.2$ with the electron density derived by Del Zanna, Landini, & Mason (2002) for Capella (G1 III + G8 III) and AU Mic (dM1e), because we use the same computation methods. The comparison tell us that at $\log T \sim 5.2$ the electron density is slightly less in α Cen A than in the more active Capella ($\log N_e \sim 10.6$) and AU Mic ($\log N_e \sim 10.7$).

(7) The emission measure distribution of α Cen A derived from emission lines of ions not in the Li and Na isoelectronic sequences is in close agreement with that of the quiet Sun in the temperature range $5.0 < \log T < 5.6$, but lies somewhat above the quiet Sun in the temperature range $4.5 < \log T < 5.0$. This could be explained by the higher metal abundance of α Cen A combined with a somewhat less active corona that provides less conductive heating to the upper transition region. The estimated total radiative power loss from the transition region ($4.4 < \log T < 5.6$) is $4.2 \times 10^5 \text{ erg s}^{-1} \text{ cm}^{-2}$, corresponding to $2.4 \times 10^{-5} L_{\text{bol}}$.

Acknowledgements. This work is supported by NASA grant S-56500-D to NIST and the University of Colorado. We thanks Dr. Joseph B. Gurman, who kindly provided us information about the UVSP/SMM solar spectrum, and Dr. Richard Shine and Dr. Zoe Frank who made it available.

References

- Ayres, T.R., Fleming, T.A., Simon, T., et al., ApJS, 96, 223
 Bevington P.R., 1969, in Data Reduction and Error Analysis for the Physical Science (New York: McGraw-Hill)
 Bohlin, R.C., Dickinson, M/E., & Calzetti, D. 2001, AJ, 122, 2118
 Boesgaard, A.M., Hagen, W., 1974, ApJ 189, 85
 Brage, T., Judge, P.G., & Brekke, P. 1996, ApJ, 464, 1030
 Brekke, P. 1993, ApJ, 408, 735
 Brekke, P. 1993, ApJS, 87, 443
 Brekke, P., Thompson, W.T., Woods, T.N., & Eparvier, F.G., ApJ, 536, 959
 Bruner, M.E., & McWhirter, R.W.P. 1988, ApJ, 326, 1002.
 Chae, J., Yun, H.S., & Poland, A.I. 1998, ApJS, 114, 151
 Cook, J.W., Keenan, F.P., Dufton, P.L., et al., 1995, ApJ, 444, 936
 Curdt, W., Brekke, P., Feldman U., et al., 2001, A&A, 375, 591
 Del Zanna, G., Landini, M., & Mason, H.E. 2002, A&A, 385, 968
 Dere, K.P., Bartoe, J.-D.F., & Brueckner, G.E. 1989, Sol. Phys., 123, 41
 Dere, K.P., Landi, E., Mason, H.E., Monsignori Fossi, B.C., Young, P.R. 1997, A&AS, 125, 149
 Dere, K.P., & Mason, H.E. 1981, in Solar Active Regions, ed. F.Q. Orrall, Colorado Univ. Press, 129
 Dere, K.P., & Mason, H.E. 1993, Sol. Phys., 144, 217
 Dufton, P.L., Hibbert, A., Kingston, A.E., & Doschek, G.A. 1982, ApJ, 258, 548
 Feldman, U., Doschek, G.A., VanHoosier, M.E., & Tousey, R. 1975, ApJ, 199, L67
 Feldman, U., Behring, W.E., Curdt, W., Schühle, U., Wilhelm, K., Lemaire, P., & Moran, T.M. 1997, ApJSS, 113, 195
 Feltzing, S., Gonzalez, G. 2001, A&A, 367, 253
 Grevesse, N., & Sauval, A.J. 1998, Space Science Reviews, 85, 161
 Guenther D.B. & Demarque P. 2000, ApJ, 531, 503
 Hallam, K.L., Altner, B., Endal, A.S., 1991, ApJ, 372, 610
 Harper, G. M., Jordan, C., Judge, P. G., Robinson, R. D., Carpenter, K. G., & Brage, T. 1999, MNRAS, 303, L41
 Jordan, C. 1967, Sol. Phys., 2, 441
 Jordan, C. 1975, MNRAS, 170, 429
 Jordan, C., & Brown, A. 1981, in Solar Phenomena in Stars and Stellar Systems, ed. R.M. Bonnet and A.K. Dupree (Dordrecht: Reidel), 199
 Jordan, C., Ayres, T.R., Brown, A., Linsky, J.L., Simon, T. 1987, MNRAS, 225, 903
 Judge, P.G., Woods, T.N., Brekke, P., & Rottman, G.J. 1995, ApJ, 455, L85
 Kelly, R.L. 1982, in Atomic and Ionic Spectrum Lines Below 200 Å, ORNL-592
 Kimble, R.A., et al. 1998, ApJ, 492, L83

- Landi, E. & Landini, M. 1997, A&A, 327, 1230
- Landi, E. & Landini, M. 1998, A&A, 340, 265
- Leitherer, C., et al. 2001, "STIS Instrument Handbook", Version 5.1, (Baltimore: STScI).
- Lindler D. 1999a, Communication presented at the STSI IDT meeting, Feb. 11, 1999.
- Lindler D. 1999b, STIS Post-Launch Quick-Look Analysis and SMOV Reports #62.
- Linsky, J.L., & Wood, B.E. 1994, ApJ, 430, 342
- Linsky, J.L., Wood, B.E., Judge P., Brown, A., Andrulis, C., & Ayres, T.R. 1995, ApJ, 442, 381
- Linsky, J.L., Wood B.E. 1996, ApJ, 463, 254
- Linsky, J.L., Wood, B.E., Brown, A., & Osten, R.A. 1998, ApJ, 492, 767
- Mauas, P.J., , Avrett, E.H., & Loeser, R., 1989, ApJ, 345, 1104
- Mazzotta, P., Mazzitelli, G., Colafrancesco, S., & Vittorio, N. 1998, A&AS, 133, 403
- Morel, P., Provost, J., Lebreton, Y., Thévenin, F., and Berthomieu, G. 2000, A&A, 363, 675
- Neff, J.E., Walter, F.M., Rodonò, M., & Linsky, J.L. 1989, A&A, 215, 79
- Pagano, I., Linsky, J.L., Carkner, L., Robinson, R.D., Woodgate, B., & Timothy G. 2000, ApJ, 532, 497
- Pagano, I., Linsky, J.L., Curdt, W., et al., in preparation
- Perryman, M.A.C., et al., 1997, A&A, 323, L49
- Peter, H. 2001, A&A, 374, 1108
- Pourbaix, D., Neuforge-Verheeecke, C., & Noels, A. 1999, A&A, 344, 172
- Pourbaix, D. et al. 2002, A&A, 386, 280
- Raassen, A.J.J., Ness, J.-U., Mewe, R., van der Meer, R.L.J., Burwitz, V., & Kaastra, J.S. 2003, A&A, in press
- Redfield, S., Linsky, J.L., Ake, T.B., Ayres, T.R., Dupree, A.K.; Robinson, R.D., Wood, B.E., Young, P.R. 2002, ApJ, 581, 626
- Rosner, R., Tucker, W.H., and Vaiana, G.S. 1978, ApJ, 220, 643
- Rottman, G.J., Woods, T.N., & Sparn, T.P. 1993, J. Geophys. Res., 98, 10667
- Roussel-Dupré, D. 1983, ApJ, 275, 892
- Saar, S.H., & Osten, R.A. 1997, MNRAS 284, 803
- Samain, D. 1991, A&A, 244, 217
- Sandlin, G.D., Bartoe, J.-D.F., Brueckner, G.E., Tousey, R., & VanHoosier, M.E. 1986, ApJS, 61, 801
- Shine, R., & Frank, Z. 2000, data retrivable from *ftp* : [//umbra.nascom.nasa.gov/pub/uv_atlases/](http://umbra.nascom.nasa.gov/pub/uv_atlases/).
- Teriaca, L., Banerjee, D., Doyle, J.G. 1999, A&A, 349, 636
- Wilhelm, K., Lemaire, P., & Dammasch, I.E., 1998, A&A, 334, 685
- Wilhelm, K., Woods, T.N., Schühle, U., et al., 1999, A&A, 352, 321
- Wood, B.E. 1996, Ph.D. Thesis, University of Colorado
- Wood, B.E., Linsky, J.L., & Ayres, T.R. 1997, ApJ, 478, 745
- Wood, B.E., Linsky, J.L., Müller, H.-R., Zank, G. 2001, ApJ, 547, L49
- Woods, T.N., & Rottman, G.J. 1990, J. Geophys. Res., 95, 6227
- Woodgate, B.E. et al. 1980, Sol. Phys., 65, 73
- Woodgate, B.E., et al. 1998, PASP, 110, 1183
- Young, P.R., Del Zanna, G., Landi, E., Dere, K.E., Mason, H.E., Landini, M 2003, ApJS, 144, 135.
- Zirin, H. 1975, ApJ, 199, L63

Table 4. Line identifications, velocity shifts, FWHM, and fluxes.

Line ^a ID	Lab Wavelength (Å)	Observed Wavelength (Å)	Velocity ^b Shift km s ⁻¹	Flux (10 ⁻¹⁵) erg cm ⁻² s ⁻¹	FWHM ^c km s ⁻¹	Notes ^d
C III	1174.933	1174.8595 ± 0.0009	4.7 ± 0.2	162.0 ± 3.7	47.7 ± 0.4	emd
C III	1175.263	1175.1910 ± 0.0008	5.1 ± 0.2	125.2 ± 3.8	49.1 ± 0.5	emd
C III	1175.590	1175.4908 ± 0.0070	-1.8 ± 1.8	111.2 ± 7.1	49.5 ± 0.4	emd
C III	1175.711	1175.6449 ± 0.0031	6.6 ± 0.8	402.2 ± 4.7	48.4 ± 0.4	emd
C III	1175.987	1175.9141 ± 0.0008	4.8 ± 0.2	114.0 ± 3.7	48.0 ± 0.7	emd
C III	1176.370	1176.2869 ± 0.0008	2.3 ± 0.2	155.8 ± 3.9	51.2 ± 1.8	emd
Si II	1190.416	1190.3302 ± 0.0009	1.8 ± 0.2	37.7 ± 3.0	39.5 ± 0.5	emd, ISM
Si II	1193.289	1193.2031 ± 0.0008	1.9 ± 0.2	23.6 ± 4.3	56.0 ± 0.4	emd, ISM
S III+ C I	1194.020/.064	1193.9884 ± 0.0008		17.8 ± 4.5	59.1 ± 0.5	
Si II	1194.500	1194.4117 ± 0.0008	1.3 ± 0.2	53.5 ± 4.5	58.2 ± 0.4	emd
Si II	1197.394	1197.3188 ± 0.0009	4.6 ± 0.2	23.9 ± 3.5	45.5 ± 0.4	emd
S V	1199.134	1199.0846 ± 0.0007	11.1 ± 0.2	29.7 ± 4.9	64.0 ± 0.4	NIST
N I	1199.549	1199.4596 ± 0.0010	1.1 ± 0.3	55.2 ± 2.7	35.3 ± 0.5	ISM
N I	1200.224	1200.1270 ± 0.0011	-0.8 ± 0.3	48.9 ± 2.3	29.4 ± 0.5	ISM
N I	1200.711	1200.6163 ± 0.0009	-0.2 ± 0.2	27.6 ± 3.2	41.2 ± 0.5	ISM
S III	1200.966	1200.8907 ± 0.0010	4.7 ± 0.2	33.5 ± 2.9	37.4 ± 0.5	emd
		1201.3582 ± 0.0019		5.0 ± 0.8	10.2 ± 0.9	
		1201.9110 ± 0.0017		4.0 ± 0.9	11.9 ± 0.9	
		1202.5665 ± 0.0019		7.1 ± 0.8	10.1 ± 0.9	
S I	1203.440	1203.3491 ± 0.0026	0.8 ± 0.6	3.0 ± 0.4	5.5 ± 1.3	Kelly (1982)
S V + S I	1204.300/.33	1204.2095 ± 0.0013		19.0 ± 1.7	21.7 ± 0.6	Curd et al. (2001)
		1204.3019 ± 0.0016		7.2 ± 1.1	13.9 ± 0.8	
		1205.0609 ± 0.0021		2.3 ± 0.6	8.0 ± 1.0	
S I	1205.565	1205.4757 ± 0.0086	1.3 ± 2.1	10.3 ± 3.4	15.9 ± 6.5	
Si III	1206.510	1206.4255 ± 0.0010	2.5 ± 0.2	1893.0 ± 4.1	53.0 ± 1.0	emd, NC+BC
S I	1207.015	1206.9293 ± 0.0023	2.2 ± 0.6	4.2 ± 0.5	7.1 ± 1.1	
		1207.0967 ± 0.0030		1.9 ± 0.3	4.0 ± 1.5	Sandlin-1 1207.21
		1207.6364 ± 0.0013		6.6 ± 1.6	21.2 ± 0.6	Sandlin-1 1207.71
P I	1208.430	1208.3192 ± 0.0025	-4.0 ± 0.6	3.0 ± 0.5	6.0 ± 1.2	NIST
S I	1208.850	1208.7595 ± 0.0013	1.0 ± 0.3	13.0 ± 1.6	20.6 ± 0.7	
S I	1211.212	1211.1201 ± 0.0013	0.7 ± 0.3	9.4 ± 1.7	22.7 ± 0.6	
Ly alpha	1215.670	1215.5780 ± 0.0005	0.8 ± 0.1	104377.8 ± 333.3	155.4 ± 0.5	NIST, multi comp.
O V	1218.344	1218.2682 ± 0.0008	4.8 ± 0.2	266.9 ± 13.3	55.3 ± 1.9	NIST
		1227.9579 ± 0.0020		5.5 ± 0.7	9.4 ± 1.0	
S I	1229.608	1229.5201 ± 0.0019	2.0 ± 0.5	2.6 ± 0.8	11.0 ± 0.9	
N V	1238.821	1238.7335 ± 0.0032	2.3 ± 0.8	287.0 ± 3.7	48.4 ± 0.4	NC+BC, ISM
S I	1241.905	1241.8154 ± 0.0020	1.8 ± 0.5	1.8 ± 0.7	9.2 ± 1.0	
Fe XII	1242.000	1241.8970 ± 0.0011	-1.4 ± 0.3	6.3 ± 2.6	33.3 (imposed)	
C I	1242.230	1242.1324 ± 0.0039	-0.1 ± 0.9	1.0 ± 0.3	UL	
		1242.3331 ± 0.0020		1.7 ± 0.7	9.5 ± 1.0	
		1242.4186 ± 0.0014		6.9 ± 1.5	19.5 ± 0.7	
N V	1242.804	1242.7261 ± 0.0017	4.7 ± 0.4	141.7 ± 4.0	52.1 ± 0.4	ISM
N I+ C I	1243.180/.14	1243.0596 ± 0.0020		9.7 ± 1.9	24.8 ± 2.6	
N I	1243.307	1243.2079 ± 0.0021	-0.5 ± 0.5	6.0 ± 1.8	22.9 ± 0.6	
C I	1243.518	1243.4125 ± 0.0013	-2.0 ± 0.3	5.4 ± 1.7	22.5 ± 0.6	Kelly (1982)
C I	1243.784	1243.6854 ± 0.0018	-0.3 ± 0.4	2.0 ± 0.9	12.0 ± 0.9	Kelly (1982)
C I	1243.998	1243.8966 ± 0.0017	-1.0 ± 0.4	4.8 ± 1.0	13.4 ± 0.8	Kelly (1982)
Ca II + C I	1244.060/.127	1244.0105 ± 0.0014		2.6 ± 1.6	20.4 ± 0.7	
C I	1244.535	1244.4336 ± 0.0016	-1.0 ± 0.4	7.2 ± 1.2	16.1 ± 0.7	Kelly (1982)
C I + Ca II	1244.996/.99	1244.8947 ± 0.0017		3.2 ± 1.0	12.7 ± 0.8	Kelly (1982) (C I)
C I	1245.183	1245.0857 ± 0.0016	0.0 ± 0.4	5.0 ± 1.2	15.1 ± 0.8	Kelly (1982)

Table 4—Continued

Line ^a ID	Lab Wavelength (Å)	Observed Wavelength (Å)	Velocity ^b Shift km s ⁻¹	Flux (10 ⁻¹⁵) erg cm ⁻² s ⁻¹	FWHM ^c km s ⁻¹	Notes ^d
C I	1245.538	1245.4320 ± 0.0016	-2.1 ± 0.4	3.8 ± 1.2	16.1 ± 0.7	Kelly (1982)
C I	1245.943	1245.8478 ± 0.0016	0.5 ± 0.4	7.7 ± 1.2	15.1 ± 0.8	Kelly (1982)
C I	1246.180	1246.0800 ± 0.0018	-0.6 ± 0.4	3.6 ± 1.0	12.7 ± 0.8	Kelly (1982)
		1246.5189 ± 0.0039		1.0 ± 0.2	UL	
C I	1246.862	1246.7611 ± 0.0016	-0.8 ± 0.4	8.9 ± 1.2	15.9 ± 0.7	Kelly (1982)
C I	1246.940	1246.8567 ± 0.0029	3.4 ± 0.7	1.2 ± 0.4	4.7 ± 1.4	
S I	1247.160	1247.0626 ± 0.0018	0.0 ± 0.4	5.2 ± 0.9	12.0 ± 0.9	
C III	1247.383	1247.2896 ± 0.0010	1.0 ± 0.2	6.2 ± 3.3	42.5 ± 0.5	emd
C I	1247.867	1247.7620 ± 0.0015	-1.8 ± 0.4	7.1 ± 1.3	16.3 ± 0.7	Kelly (1982)
C I	1248.009	1247.9132 ± 0.0015	0.4 ± 0.4	9.9 ± 1.4	18.3 ± 0.7	Kelly (1982)
C I	1249.004	1248.9060 ± 0.0016	-0.1 ± 0.4	6.6 ± 1.1	14.6 ± 0.8	Kelly (1982)
C I	1249.405	1249.3002 ± 0.0014	-1.7 ± 0.3	12.3 ± 1.5	19.1 ± 0.7	Kelly (1982)
C I + Si II	1250.423/.433	1250.3245 ± 0.0014		9.7 ± 1.5	20.1 ± 0.7	Kelly (1982) (C I)
S II	1250.584	1250.4974 ± 0.0013	2.7 ± 0.3	15.5 ± 1.9	24.9 ± 0.6	emd
Si II + C I	1251.164/.176	1251.0778 ± 0.0014		13.7 ± 1.5	19.6 ± 0.7	Kelly (1982) (C I)
C I	1252.200	1252.1028 ± 0.0016	0.2 ± 0.4	7.8 ± 1.1	14.5 ± 0.8	
S I	1253.325	1253.2291 ± 0.0022	0.5 ± 0.5	2.1 ± 0.6	8.2 ± 1.0	
C I	1253.467	1253.3693 ± 0.0013	0.1 ± 0.3	19.1 ± 1.7	22.2 ± 0.6	
S II	1253.811	1253.7173 ± 0.0012	1.0 ± 0.3	29.8 ± 2.0	26.5 ± 0.6	emd, NIST
C I	1254.513	1254.4180 ± 0.0015	0.8 ± 0.4	10.4 ± 1.3	17.1 ± 0.7	Kelly (1982)
Si I	1255.276	1255.1732 ± 0.0013	-1.1 ± 0.3	10.9 ± 1.7	22.6 ± 0.6	
		1255.2924 ± 0.0013		2.4 ± 1.7	21.7 ± 2.1	Sandlin-1 1255.42
		1256.0272 ± 0.0013		2.6 ± 1.8	23.8 ± 0.6	
C III + C I	1256.470/.498	1256.3893 ± 0.0011		37.0 ± 2.5	32.3 ± 0.5	
C I	1257.565	1257.4651 ± 0.0015	-0.4 ± 0.4	10.4 ± 1.3	17.1 ± 0.7	
Si I	1258.795	1258.6921 ± 0.0011	-1.1 ± 0.3	38.3 ± 2.5	32.1 ± 0.5	
S II	1259.530	1259.4275 ± 0.0012	-1.0 ± 0.3	49.5 ± 2.2	29.2 ± 0.5	emd
Si II	1260.421	1260.3027 ± 0.0009	-4.7 ± 0.2	82.0 ± 4.0	51.4 ± 0.4	CR, emd, ISM
C I	1260.613	1260.5212 ± 0.0018	1.6 ± 0.4	10.9 ± 1.0	12.8 ± 0.8	
C I	1260.927	1260.8337 ± 0.0016	1.3 ± 0.4	2.7 ± 1.2	15.6 ± 0.8	
Ca VII	1261.070	1260.9786 ± 0.0011	1.7 ± 0.3	6.4 ± 2.6	33.5 ± 0.5	Feldman et al. (1997)
C I	1261.719	1261.6206 ± 0.0016	0.1 ± 0.4	12.7 ± 1.2	16.1 ± 0.7	
S I	1262.860	1262.7614 ± 0.0020	0.0 ± 0.5	2.9 ± 0.8	10.1 ± 0.9	
Si II	1264.737	1264.6426 ± 0.0009	1.1 ± 0.2	225.9 ± 3.9	50.2 ± 0.4	emd, CR
Si II	1265.001	1264.9167 ± 0.0011	3.5 ± 0.3	65.8 ± 2.4	31.5 ± 0.5	emd, CR
Fe II	1265.639	1265.5498 ± 0.0017	2.3 ± 0.4	1.7 ± 1.1	13.7 ± 0.8	
C I	1266.270	1266.1687 ± 0.0015	-0.5 ± 0.4	12.0 ± 1.4	18.2 ± 0.7	
C I	1266.415	1266.3159 ± 0.0016	-0.0 ± 0.4	21.7 ± 1.2	15.6 ± 0.8	
C I	1266.517	1266.4181 ± 0.0016	0.0 ± 0.4	6.1 ± 1.2	15.8 ± 0.7	
C I	1266.604	1266.5135 ± 0.0018	2.0 ± 0.4	3.3 ± 0.9	12.2 ± 0.8	
C I	1267.596	1267.4885 ± 0.0014	-2.0 ± 0.3	16.0 ± 1.7	21.5 ± 0.6	
C I	1268.051	1267.9519 ± 0.0017	0.0 ± 0.4	1.9 ± 1.1	14.7 ± 0.8	Kelly (1982)
S I	1269.209	1269.1121 ± 0.0020	0.6 ± 0.5	2.1 ± 0.8	10.5 ± 0.9	
Fe II	1269.353	1269.2498 ± 0.0029	-0.9 ± 0.7	1.0 ± 0.4	4.9 ± 1.3	
S I	1270.782	1270.6803 ± 0.0018	-0.5 ± 0.4	12.9 ± 1.0	13.1 ± 0.8	
S I	1272.075	1271.9768 ± 0.0153	0.3 ± 3.6	2.0 ± 1.0	13.6 ± 0.8	
Fe II + Fe II	1272.613/.655	1272.5409 ± 0.0015		3.1 ± 1.7	22.4 ± 0.6	
C I	1274.109	1274.0189 ± 0.0014	2.3 ± 0.3	4.5 ± 1.6	20.5 ± 0.7	
C I	1274.756	1274.6608 ± 0.0017	1.1 ± 0.4	10.8 ± 1.1	14.1 ± 0.8	
C I	1274.984	1274.8885 ± 0.0016	1.0 ± 0.4	25.4 ± 1.3	16.8 ± 0.7	
C I	1275.288	1275.1871 ± 0.0019	-0.3 ± 0.4	4.9 ± 0.9	11.1 ± 0.9	Kelly (1982)

Table 4—Continued

Line ^a ID	Lab Wavelength (Å)	Observed Wavelength (Å)	Velocity ^b Shift km s ⁻¹	Flux (10 ⁻¹⁵) erg cm ⁻² s ⁻¹	FWHM ^c km s ⁻¹	Notes ^d
Fe II	1275.807	1275.6993 ± 0.0015	-1.8 ± 0.4	2.0 ± 1.3	17.3 ± 0.7	
C I	1276.287	1276.1793 ± 0.0013	-1.8 ± 0.3	17.6 ± 1.8	22.9 ± 0.6	
C I	1276.483	1276.3953 ± 0.0018	2.8 ± 0.4	1.7 ± 1.0	13.1 ± 0.8	
C I + Fe II	1276.750/.801	1276.6709 ± 0.0013		4.0 ± 1.9	25.2 ± 0.9	
C I	1277.042	1276.9420 ± 0.0018	-0.0 ± 0.4	2.9 ± 1.0	12.6 ± 0.8	
C I + C I	1277.245/.283	1277.1478 ± 0.0010		12.2 ± 3.4	44.3 ± 0.6	
C I + C I	1277.513/.550	1277.4358 ± 0.0010		11.0 ± 2.9	38.1 ± 0.5	
C I	1277.723	1277.6309 ± 0.0012	1.8 ± 0.3	7.7 ± 2.3	29.7 ± 0.5	
C I	1277.954	1277.8563 ± 0.0014	0.5 ± 0.3	6.3 ± 1.5	20.0 ± 0.7	
C I	1279.056	1278.9625 ± 0.0013	1.5 ± 0.3	7.2 ± 1.7	22.5 ± 0.6	
C I	1279.228	1279.1331 ± 0.0013	1.2 ± 0.3	9.1 ± 2.0	25.4 ± 0.6	CR
C I	1279.498	1279.3999 ± 0.0015	0.5 ± 0.3	6.5 ± 1.5	19.2 ± 0.7	
C I	1279.890	1279.7957 ± 0.0012	1.3 ± 0.3	9.7 ± 2.2	29.0 ± 1.1	CR
C I	1280.135	1280.0341 ± 0.0042	-0.2 ± 1.0	5.8 ± 1.9	24.1 ± 0.6	CR
C I + C I	1280.333/.404	1280.2679 ± 0.0009		10.4 ± 3.5	45.5 ± 2.1	CR
C I	1280.597	1280.5023 ± 0.0012	1.3 ± 0.3	6.5 ± 2.1	27.1 ± 0.6	CR
C I	1280.847	1280.7476 ± 0.0012	0.2 ± 0.3	6.5 ± 2.2	28.0 ± 0.6	CR
C I	1287.608	1287.5009 ± 0.0017	-1.5 ± 0.4	1.9 ± 1.1	14.4 ± 0.8	
C I	1288.037	1287.9391 ± 0.0016	0.7 ± 0.4	11.4 ± 1.2	16.0 ± 0.7	
C I	1288.422	1288.3242 ± 0.0015	0.7 ± 0.3	26.4 ± 1.5	19.7 ± 0.7	
C I	1288.710	1288.6100 ± 0.0018	0.2 ± 0.4	6.4 ± 1.0	12.7 ± 0.8	
C I	1288.917	1288.8190 ± 0.0018	0.7 ± 0.4	6.5 ± 1.0	12.9 ± 0.8	
C I	1289.891	1289.7894 ± 0.0019	-0.2 ± 0.4	4.9 ± 0.9	11.8 ± 0.9	
C I	1289.977	1289.8774 ± 0.0016	0.3 ± 0.4	14.8 ± 1.3	16.7 ± 0.7	
C I	1291.304	1291.2072 ± 0.0018	1.0 ± 0.4	6.5 ± 1.0	12.4 ± 0.8	
Si III	1294.543	1294.4680 ± 0.0009	6.1 ± 0.2	15.4 ± 3.9	50.5 ± 0.9	emd
S I	1295.653	1295.5519 ± 0.0016	0.1 ± 0.4	19.9 ± 1.3	17.1 ± 0.7	
Fe II	1296.084	1295.9924 ± 0.0017	2.3 ± 0.4	6.2 ± 1.2	15.4 ± 0.8	
S I	1296.174	1296.0760 ± 0.0017	0.8 ± 0.4	10.6 ± 1.1	13.8 ± 0.8	
Fe II	1296.287	1296.1783 ± 0.0016	-1.7 ± 0.4	2.9 ± 1.2	15.8 ± 0.7	
Si III	1296.726	1296.6675 ± 0.0011	9.9 ± 0.3	9.6 ± 2.7	35.1 ± 0.5	emd
		1297.3766 ± 0.0026		1.0 ± 0.5	6.3 ± 1.2	
Si III + Si III	1298.891/.960	1298.8571 ± 0.0009		49.8 ± 3.7	47.6 ± 1.0	
Fe II	1299.432	1299.3300 ± 0.0014	-0.1 ± 0.3	4.0 ± 1.8	23.0 ± 1.0	
S I	1300.907	1300.8074 ± 0.0018	0.5 ± 0.4	60.4 ± 1.1	13.8 ± 0.8	
O I	1302.169	1302.0695 ± 0.0011	0.5 ± 0.3	806.8 ± 2.6	33.8 ± 0.5	ISM, CR
S I	1302.865	1302.7617 ± 0.0016	-0.3 ± 0.4	12.0 ± 1.4	17.7 ± 0.7	
S I	1303.111	1303.0084 ± 0.0018	-0.1 ± 0.4	6.3 ± 1.0	13.0 ± 0.8	
Si III	1303.320	1303.2518 ± 0.0030	7.8 ± 0.7	16.3 ± 3.2	42.0 ± 1.1	emd
S I	1303.430	1303.3414 ± 0.0025	3.1 ± 0.6	1.6 ± 0.5	6.8 ± 2.2	
Fe II	1303.898	1303.7935 ± 0.0022	-0.6 ± 0.5	1.0 ± 0.7	8.9 ± 1.0	
Si II	1304.372	1304.2780 ± 0.0012	1.8 ± 0.3	73.9 ± 2.5	31.9 ± 0.5	emd, ISM, CR
O I	1304.858	1304.7607 ± 0.0011	1.1 ± 0.3	855.9 ± 2.6	34.0 ± 0.5	CR
H ₂	1305.520	1305.4186 ± 0.0018	0.2 ± 0.4	1.4 ± 1.0	12.9 ± 1.0	
Si II	1305.590	1305.4906 ± 0.0017	0.6 ± 0.4	2.7 ± 1.1	14.3 ± 0.8	
Ca II	1305.670	1305.5581 ± 0.0016	-2.3 ± 0.4	2.8 ± 1.3	16.3 ± 0.7	
O I	1306.029	1305.9283 ± 0.0012	0.3 ± 0.3	886.7 ± 2.2	29.1 ± 0.5	CR
Si II	1309.277	1309.1708 ± 0.0011	-0.9 ± 0.3	73.3 ± 2.6	34.1 ± 0.5	emd, CR
		1309.2540 ± 0.0020		22.4 ± 1.2	11.2 ± 0.9	
		1309.2947 ± 0.0013		22.0 ± 2.0	26.2 ± 0.6	
S I + C I	1310.194/.187	1310.0883 ± 0.0017		4.0 ± 1.1	14.0 ± 0.8	

Table 4—Continued

Line ^a ID	Lab Wavelength (Å)	Observed Wavelength (Å)	Velocity ^b Shift km s ⁻¹	Flux (10 ⁻¹⁵) erg cm ⁻² s ⁻¹	FWHM ^c km s ⁻¹	Notes ^d
N I	1310.540	1310.4359 ± 0.0018	-0.4 ± 0.4	4.8 ± 1.1	13.9 ± 0.8	
C I	1310.637	1310.5370 ± 0.0016	0.6 ± 0.4	12.3 ± 1.2	16.2 ± 0.7	
N I	1310.943	1310.8312 ± 0.0015	-2.1 ± 0.3	3.9 ± 1.5	19.2 ± 0.7	
C I	1311.363	1311.2642 ± 0.0014	0.8 ± 0.3	27.9 ± 1.6	21.2 ± 0.6	
C I	1311.924	1311.8195 ± 0.0018	-0.4 ± 0.4	9.2 ± 1.0	13.4 ± 0.8	
C I	1312.247	1312.1479 ± 0.0018	0.8 ± 0.4	8.3 ± 1.0	13.6 ± 0.8	
Si III	1312.590	1312.5122 ± 0.0010	5.7 ± 0.2	5.6 ± 3.3	42.8 ± 0.5	emd
C I	1312.853	1312.7582 ± 0.0020	1.8 ± 0.4	1.3 ± 0.9	11.3 ± 0.9	Kelly (1982)
Si I	1313.249	1313.1505 ± 0.0025	1.0 ± 0.6	1.7 ± 0.5	7.0 ± 1.3	
C I	1313.387	1313.2832 ± 0.0022	-0.2 ± 0.5	3.6 ± 0.7	9.2 ± 1.0	
C I	1313.464	1313.3593 ± 0.0016	-0.5 ± 0.4	17.7 ± 1.3	16.4 ± 0.7	
C I	1315.919	1315.8174 ± 0.0018	0.3 ± 0.4	13.3 ± 1.1	14.1 ± 0.8	
Si I	1316.542	1316.4344 ± 0.0019	-1.0 ± 0.4	16.9 ± 0.9	12.0 ± 0.9	
Si I	1316.618	1316.5028 ± 0.0017	-2.8 ± 0.4	12.9 ± 1.2	15.9 ± 0.7	
Ni II	1317.220	1317.1240 ± 0.0013	1.6 ± 0.3	20.2 ± 2.0	25.5 ± 0.6	
N I + N I	1318.998/9.005	1318.8418 ± 0.0019		55.1 ± 1.0	12.6 ± 0.8	
N I	1319.669/.676	1319.5709 ± 0.0020		3.3 ± 0.9	11.3 ± 0.9	
Si I	1323.515	1323.4136 ± 0.0018	0.5 ± 0.4	15.8 ± 1.0	13.1 ± 0.8	
C II+CII+CII+CII	1323.862/.906/.951/.	1323.8492 ± 0.0010		9.1 ± 3.6	47.2 ± 0.4	
N I + N I	1326.564/.571	1326.4661 ± 0.0020		1.1 ± 0.9	11.3 ± 0.9	
Si I	1326.643	1326.5382 ± 0.0018	-0.2 ± 0.4	10.1 ± 1.0	13.0 ± 0.8	
C I	1328.833	1328.7305 ± 0.0013	0.3 ± 0.3	19.6 ± 2.1	27.5 ± 0.6	CR
C I + C I	1329.085/.12	1329.0032 ± 0.0011		20.6 ± 3.0	38.4 ± 0.5	CR
C I + C I	1329.578/.60	1329.4865 ± 0.0012		23.3 ± 3.3	42.5 ± 0.5	CR
C II	1334.532	1334.4385 ± 0.0010	2.4 ± 0.2	1335.3 ± 3.3	43.3 ± 0.5	emd, ISM, CR
Ni II	1335.203	1335.1115 ± 0.0013	2.9 ± 0.3	10.1 ± 2.1	27.7 ± 0.8	
C II	1335.708	1335.6040 ± 0.0010	0.1 ± 0.2	1846.7 ± 3.7	47.8 ± 0.4	emd, CR
		1346.9371 ± 0.0018		3.1 ± 1.1	13.6 ± 0.8	
Cl I	1351.657	1351.5510 ± 0.0019	-0.1 ± 0.4	123.1 ± 0.9	12.3 ± 0.8	
C I	1354.288	1354.1864 ± 0.0016	1.0 ± 0.4	10.9 ± 1.4	17.9 ± 0.7	
O I	1355.598	1355.4945 ± 0.0019	0.6 ± 0.4	188.2 ± 1.0	13.0 ± 0.8	
C I	1355.844	1355.7443 ± 0.0014	1.4 ± 0.3	30.4 ± 1.8	23.6 ± 0.6	
S III	1357.000	1356.8817 ± 0.0015	-2.7 ± 0.3	3.6 ± 1.6	21.3 ± 0.6	Feldman et al. (1997)
C I	1357.134	1357.0287 ± 0.0016	0.2 ± 0.4	11.8 ± 1.3	17.4 ± 0.7	
C I	1357.659	1357.5486 ± 0.0019	-0.9 ± 0.4	12.3 ± 1.0	13.4 ± 0.8	
C I	1358.188	1358.0848 ± 0.0020	0.7 ± 0.4	4.2 ± 0.9	11.2 ± 0.9	
O I	1358.512	1358.4089 ± 0.0019	0.7 ± 0.4	57.2 ± 1.0	12.5 ± 0.8	
		1358.6658 ± 0.0017		6.9 ± 1.3	16.5 ± 0.7	Sandlin-1 1358.76
C I	1359.275	1359.1742 ± 0.0018	1.2 ± 0.4	21.6 ± 1.1	14.7 ± 0.8	
C I	1359.438	1359.3291 ± 0.0018	-0.6 ± 0.4	7.5 ± 1.1	14.9 ± 0.8	
Fe II	1360.170	1360.0717 ± 0.0016	1.8 ± 0.4	6.6 ± 1.4	17.8 ± 0.7	
Fe II	1361.373	1361.2697 ± 0.0017	0.7 ± 0.4	24.9 ± 1.3	16.5 ± 0.7	
Fe II	1362.748	1362.6617 ± 0.0017	4.5 ± 0.4	2.0 ± 1.3	16.7 ± 1.5	
Cl I	1363.447	1363.3184 ± 0.0022	-4.8 ± 0.5	1.7 ± 0.8	9.8 ± 0.9	
C I	1364.164	1364.0587 ± 0.0017	0.3 ± 0.4	25.3 ± 1.3	16.7 ± 0.7	
Fe II	1364.384	1364.2802 ± 0.0019	0.6 ± 0.4	5.0 ± 1.0	12.6 ± 0.8	
		1366.2848 ± 0.0019		2.2 ± 1.0	13.6 ± 0.8	Sandlin-1 1366.399
Fe II	1368.098	1367.9940 ± 0.0018	0.7 ± 0.4	10.6 ± 1.1	14.6 ± 0.8	
Fe II + ??	1368.575/.	1368.4342 ± 0.0011		3.0 ± 2.8	36.2 ± 0.5	
Fe II	1369.707	1369.6001 ± 0.0019	0.0 ± 0.4	3.3 ± 1.0	12.6 ± 0.8	
Fe II	1369.856	1369.7393 ± 0.0023	-2.1 ± 0.5	1.6 ± 0.7	8.9 ± 1.0	

Table 4—Continued

Line ^a ID	Lab Wavelength (Å)	Observed Wavelength (Å)	Velocity ^b Shift km s ⁻¹	Flux (10 ⁻¹⁵) erg cm ⁻² s ⁻¹	FWHM ^c km s ⁻¹	Notes ^d
Ni II	1370.136	1370.0336 ± 0.0014	1.0 ± 0.3	18.6 ± 1.8	23.3 ± 1.0	ISM
O V	1371.292	1371.2152 ± 0.0009	6.7 ± 0.2	21.5 ± 4.2	54.9 ± 0.4	emd
Fe II	1372.292	1372.1858 ± 0.0017	0.2 ± 0.4	7.3 ± 1.3	16.4 ± 0.7	
Fe V	1373.967	1373.8687 ± 0.0142	2.0 ± 3.1	2.0 ± 1.1	10.3 ± 1.5	
Fe V	1374.116	1373.9980 ± 0.0242	-2.3 ± 5.3	5.9 ± 1.2	16.0 ± 1.5	
		1375.1185 ± 0.0015		4.7 ± 1.7	22.1 ± 1.5	
Fe II	1376.672	1376.5645 ± 0.0022	0.0 ± 0.5	4.4 ± 0.8	9.9 ± 0.9	
Fe II	1379.615	1379.5089 ± 0.0020	0.4 ± 0.4	9.6 ± 0.9	11.9 ± 0.9	
Ni II	1381.295	1381.1951 ± 0.0016	1.8 ± 0.3	12.6 ± 1.5	19.8 ± 0.7	
S I	1381.552	1381.4512 ± 0.0025	1.6 ± 0.5	1.8 ± 0.6	7.7 ± 1.1	
S I	1385.510	1385.3998 ± 0.0043	-0.4 ± 0.9	1.0 ± 0.2		UL
Fe II	1387.219	1387.1168 ± 0.0019	1.4 ± 0.4	7.0 ± 1.0	13.5 ± 0.8	
		1388.0889 ± 0.0027		1.3 ± 0.5	6.8 ± 1.1	
S I	1388.435	1388.3315 ± 0.0020	1.1 ± 0.4	5.4 ± 0.9	11.6 ± 0.9	
S I	1389.154	1389.0481 ± 0.0026	0.6 ± 0.6	1.4 ± 0.5	7.1 ± 1.1	
Cl I	1389.693	1389.5710 ± 0.0021	-2.9 ± 0.4	1.5 ± 0.9	11.1 ± 0.9	
Fe II	1392.149	1392.0436 ± 0.0019	0.7 ± 0.4	4.4 ± 1.0	12.8 ± 0.8	
S I	1392.588	1392.4769 ± 0.0036	-0.5 ± 0.8	1.5 ± 0.3	3.7 ± 1.5	
Fe II	1392.817	1392.7147 ± 0.0018	1.4 ± 0.4	9.9 ± 1.2	15.0 ± 0.8	
Ni II	1393.330	1393.2372 ± 0.0013	3.5 ± 0.3	20.4 ± 2.1	27.3 ± 0.6	
Si IV	1393.755	1393.6670 ± 0.0011	4.5 ± 0.2	880.0 ± 3.3	43.4 ± 0.4	NC+BC, ISM
S I	1396.112	1396.0070 ± 0.0021	0.9 ± 0.4	4.8 ± 0.9	11.3 ± 0.9	
O IV]	1397.200	1397.1166 ± 0.0013	5.6 ± 0.3	4.7 ± 2.2	28.9 ± 0.6	(e)
		1398.6799 ± 0.0023		3.9 ± 0.7	9.5 ± 1.0	Sandlin-1 1398.76
Ni II	1399.026	1398.9144 ± 0.0020	-0.5 ± 0.4	5.4 ± 1.0	12.4 ± 0.8	
O IV]	1399.780	1399.7104 ± 0.0011	8.5 ± 0.2	17.7 ± 3.2	41.5 ± 0.5	(e)
O IV]	1401.157	1401.0774 ± 0.0010	6.4 ± 0.2	93.6 ± 3.6	46.2 ± 0.4	(e)
S I	1401.514	1401.4010 ± 0.0018	-0.7 ± 0.4	7.2 ± 1.2	15.8 ± 0.7	
Si IV	1402.770	1402.6821 ± 0.0011	4.7 ± 0.2	470.0 ± 3.2	41.9 ± 0.5	NC+BC
O IV] + S IV]	1404.806/.808	1404.7100 ± 0.0010		46.2 ± 3.7	47.5 ± 0.4	(e)
Fe II	1405.608	1405.5016 ± 0.0018	0.7 ± 0.4	7.9 ± 1.2	15.9 ± 0.7	
S IV]	1406.016	1405.9630 ± 0.0011	12.2 ± 0.2	17.1 ± 3.3	43.2 ± 0.5	(e) NIST
O IV]	1407.382	1407.3060 ± 0.0011	7.3 ± 0.2	17.7 ± 3.3	43.5 ± 0.4	(e)
		1408.0629 ± 0.0036		1.4 ± 0.4	4.9 ± 1.3	Sandlin-1 1408.18
Si II	1409.073	1408.9474 ± 0.0025	-3.3 ± 0.5	1.8 ± 0.6	8.0 ± 1.1	
S I	1409.337	1409.2207 ± 0.0020	-1.3 ± 0.4	5.9 ± 1.0	12.9 ± 0.8	
Fe II	1410.621	1410.5239 ± 0.0021	2.8 ± 0.4	3.3 ± 0.9	11.1 ± 0.9	
Ni II	1411.071	1410.9615 ± 0.0016	0.2 ± 0.3	17.0 ± 1.5	19.6 ± 0.7	
		1411.1924 ± 0.0024		2.7 ± 0.7	8.9 ± 1.0	Sandlin-1 1411.28
		1411.2964 ± 0.0029		1.3 ± 0.5	6.1 ± 1.2	Sandlin-1 1411.354
Fe II	1411.470	1411.3773 ± 0.0040	3.8 ± 0.9	1.5 ± 0.2	3.1 ± 1.7	
N I	1411.949	1411.8347 ± 0.0019	-0.8 ± 0.4	11.8 ± 1.1	14.1 ± 0.8	
Fe II	1412.834	1412.7360 ± 0.0015	2.7 ± 0.3	17.9 ± 1.7	22.7 ± 0.6	
Ni II	1414.299	1414.1871 ± 0.0014	-0.3 ± 0.3	3.3 ± 1.9	24.5 ± 0.6	
S I + Fe II	1414.873/.882	1414.7700 ± 0.0021		1.0 ± 0.9	11.2 ± 0.9	
		1414.9608 ± 0.0025		1.6 ± 0.6	7.9 ± 1.1	Sandlin-1 1415.06
		1415.4392 ± 0.0016		3.0 ± 1.5	19.9 ± 0.7	Sandlin-1 1415.564
Ni II	1415.728	1415.6165 ± 0.0019	-0.2 ± 0.4	5.8 ± 1.1	13.7 ± 0.8	
Fe II	1416.710	1416.6061 ± 0.0027	1.5 ± 0.6	3.7 ± 1.4	17.6 ± 2.6	
S IV]	1416.887	1416.8456 ± 0.0028	14.7 ± 0.6	7.4 ± 2.9	37.6 ± 5.7	(e) emd
Fe II	1417.733	1417.6129 ± 0.0023	-2.0 ± 0.5	1.4 ± 0.9	9.5 ± 4.3	

Table 4—Continued

Line ^a ID	Lab Wavelength (Å)	Observed Wavelength (Å)	Velocity ^b Shift km s ⁻¹	Flux (10 ⁻¹⁵) erg cm ⁻² s ⁻¹	FWHM ^c km s ⁻¹	Notes ^d
Fe II	1418.853	1418.7500 ± 0.0017	1.7 ± 0.4	6.5 ± 1.3	16.8 ± 1.6	
Ni II	1423.212	1423.1111 ± 0.0020	2.2 ± 0.4	4.7 ± 0.9	12.3 ± 0.8	
Fe II	1424.047	1423.9326 ± 0.0021	-0.6 ± 0.4	4.0 ± 0.9	11.9 ± 0.9	
Fe II + Fe II	1424.716/.786	1424.6141 ± 0.0015		16.0 ± 1.6	21.4 ± 0.6	
S I	1425.028	1424.9219 ± 0.0018	1.1 ± 0.4	39.6 ± 1.2	16.1 ± 0.7	
S I + S I	1425.188/.219	1425.0830 ± 0.0017		21.6 ± 1.3	16.8 ± 0.7	
		1427.0327 ± 0.0021		3.2 ± 0.9	11.7 ± 0.9	Sandlin-1 1427.14
H ₂	1430.161	1430.0469 ± 0.0017	-0.5 ± 0.4	5.6 ± 1.4	17.7 ± 0.7	
CO	1431.200	1431.1058 ± 0.0024	3.7 ± 0.5	1.4 ± 0.7	8.8 ± 1.0	
C I	1431.597	1431.4908 ± 0.0020	1.2 ± 0.4	16.9 ± 1.0	13.5 ± 0.8	
C I	1432.105	1431.9980 ± 0.0020	1.1 ± 0.4	20.6 ± 1.0	12.9 ± 0.8	
C I	1432.530	1432.4227 ± 0.0017	1.0 ± 0.4	14.6 ± 1.3	17.3 ± 0.7	
Fe II	1432.875	1432.7649 ± 0.0022	0.4 ± 0.5	3.5 ± 0.8	10.1 ± 0.9	
		1432.9351 ± 0.0018		4.7 ± 1.2	16.0 ± 0.7	Sandlin-1 1433.04
S I	1433.279	1433.1779 ± 0.0016	2.3 ± 0.3	31.6 ± 1.5	19.4 ± 0.7	
H ₂ + H ₂	1434.079/.101	1434.0077 ± 0.0014		2.6 ± 2.0	26.5 ± 0.6	
Fe II	1434.994	1434.8807 ± 0.0016	-0.2 ± 0.3	12.6 ± 1.6	21.0 ± 0.6	
Cr II	1435.369	1435.2521 ± 0.0029	-1.0 ± 0.6	1.7 ± 0.5	6.1 ± 1.2	
CO	1436.560	1436.4437 ± 0.0022	-0.8 ± 0.5	5.2 ± 0.8	10.4 ± 0.9	
S I	1436.967	1436.8527 ± 0.0019	-0.4 ± 0.4	17.5 ± 1.1	14.5 ± 0.8	
Fe II + Fe II	1438.133/.135	1438.0145 ± 0.0023		2.9 ± 1.2	9.9 ± 0.9	
Fe II	1440.775	1440.6633 ± 0.0098	0.2 ± 2.0	4.3 ± 1.3	13.3 ± 15.6	
Fe II	1440.910	1440.8094 ± 0.0018	2.5 ± 0.4	4.9 ± 1.3	16.3 ± 4.6	
Fe II	1442.746	1442.6432 ± 0.0018	2.1 ± 0.4	8.5 ± 1.2	15.5 ± 0.8	
S I	1444.297	1444.1824 ± 0.0021	-0.3 ± 0.4	8.1 ± 0.9	11.8 ± 0.9	
Fe II	1444.981	1444.8727 ± 0.0018	1.0 ± 0.4	3.9 ± 1.3	17.0 ± 0.7	
Si VIII + CO	1445.750/.78	1445.6747 ± 0.0009		14.2 ± 4.8	62.2 ± 0.4	
Ni II	1446.589	1446.4758 ± 0.0019	-0.0 ± 0.4	5.0 ± 1.1	14.0 ± 0.8	
Fe II	1447.270	1447.1682 ± 0.0020	2.4 ± 0.4	4.6 ± 1.0	12.6 ± 0.8	Sandlin-1 1447.29
		1447.9115 ± 0.0027		2.7 ± 0.6	7.4 ± 1.1	Sandlin 1448.018
S I	1448.229	1448.1130 ± 0.0018	-0.6 ± 0.4	3.7 ± 1.3	16.7 ± 0.7	
		1449.8894 ± 0.0021		4.1 ± 0.9	12.1 ± 0.9	Sandlin-1 1449.996
Ni II	1454.852	1454.7437 ± 0.0015	1.1 ± 0.3	21.2 ± 1.9	24.3 ± 0.6	
CO	1455.290	1455.1621 ± 0.0018	-2.9 ± 0.4	2.8 ± 1.2	15.8 ± 0.7	
		1455.7979 ± 0.0015		5.7 ± 1.9	24.3 ± 0.6	Sandlin-1 1455.91
C I	1459.032	1458.9189 ± 0.0016	0.2 ± 0.3	15.0 ± 1.6	20.3 ± 0.7	
Fe II + H ₂	1459.311/.340	1459.2554 ± 0.0012		6.3 ± 2.8	36.3 ± 0.5	
C I	1460.450	1460.3446 ± 0.0018	1.8 ± 0.4	3.8 ± 1.2	16.1 ± 0.7	
C I	1461.860	1461.7498 ± 0.0020	0.8 ± 0.4	2.8 ± 1.0	13.1 ± 0.8	
C I	1463.336	1463.2236 ± 0.0014	0.4 ± 0.3	33.9 ± 2.2	28.9 ± 0.6	
C I	1463.563	1463.4458 ± 0.0019	-0.6 ± 0.4	7.3 ± 1.2	15.5 ± 0.8	
		1464.4509 ± 0.0022		3.2 ± 0.9	11.3 ± 0.9	Sandlin-1 1464.571
C I + H ₂	1464.9805.020	1464.8959 ± 0.0015		4.8 ± 1.7	22.7 ± 0.6	
		1465.3080 ± 0.0020		2.6 ± 1.0	13.6 ± 0.8	Sandlin-1 1465.410
		1466.0999 ± 0.0021		9.3 ± 0.9	11.6 ± 0.9	Sandlin-1 1466.17
Ni II	1467.265	1467.1506 ± 0.0020	0.1 ± 0.4	9.3 ± 1.0	13.4 ± 0.8	
C I	1467.402	1467.2775 ± 0.0016	-2.0 ± 0.3	20.1 ± 1.7	22.2 ± 0.6	
C I	1467.670	1467.5430 ± 0.0020	-2.5 ± 0.4	7.3 ± 1.1	13.8 ± 0.8	
Ni II	1467.762	1467.6487 ± 0.0018	0.3 ± 0.4	14.6 ± 1.3	16.9 ± 0.7	
C I	1467.877	1467.7626 ± 0.0021	0.1 ± 0.4	20.9 ± 1.0	12.4 ± 0.8	
		1467.9211 ± 0.0024		3.7 ± 0.7	9.2 ± 1.0	Sandlin-1 1468.03

Table 4—Continued

Line ^a ID	Lab Wavelength (Å)	Observed Wavelength (Å)	Velocity ^b Shift km s ⁻¹	Flux (10 ⁻¹⁵) erg cm ⁻² s ⁻¹	FWHM ^c km s ⁻¹	Notes ^d
C I	1468.410	1468.2972 ± 0.0020	0.4 ± 0.4	25.6 ± 1.0	13.2 ± 0.8	
C I	1469.110	1469.0110 ± 0.0029	3.2 ± 0.6	2.7 ± 0.5	6.4 ± 1.2	
C I	1470.094	1469.9783 ± 0.0020	-0.1 ± 0.4	28.0 ± 1.0	13.6 ± 0.8	
C I	1470.450	1470.3217 ± 0.0103	-2.7 ± 2.1	4.4 ± 1.0	12.9 ± 1.0	
S I	1471.832	1471.7147 ± 0.0024	-0.4 ± 0.5	5.9 ± 0.7	9.1 ± 1.0	
C I	1472.231	1472.1147 ± 0.0021	-0.2 ± 0.4	22.1 ± 1.0	12.5 ± 0.8	
S I	1472.972	1472.8656 ± 0.0017	1.8 ± 0.4	156.0 ± 1.4	18.3 ± 0.7	
C I	1473.242	1473.1217 ± 0.0021	-1.0 ± 0.4	6.3 ± 0.9	12.3 ± 0.8	
C I	1473.480	1473.3469 ± 0.0027	-3.6 ± 0.6	1.8 ± 0.6	7.2 ± 1.1	
Fe II + H ₂	1473.822/.834	1473.7126 ± 0.0022		2.9 ± 0.9	11.5 ± 0.9	
S I	1473.995	1473.8810 ± 0.0018	0.3 ± 0.4	86.3 ± 1.2	16.2 ± 0.7	
S I	1474.380	1474.2615 ± 0.0019	-0.7 ± 0.4	38.0 ± 1.2	15.0 ± 0.8	
S I	1474.572	1474.4551 ± 0.0023	-0.3 ± 0.5	12.5 ± 0.8	10.7 ± 0.9	
C I	1474.740	1474.6346 ± 0.0027	2.0 ± 0.6	4.7 ± 0.6	7.4 ± 1.1	
Ni II	1477.227	1477.1119 ± 0.0023	0.1 ± 0.5	7.4 ± 0.8	10.0 ± 0.9	
C I	1480.990	1480.8745 ± 0.0016	0.1 ± 0.3	7.5 ± 1.6	20.2 ± 0.7	
C I	1481.114	1481.0020 ± 0.0022	0.8 ± 0.5	11.2 ± 0.8	11.0 ± 0.9	
S I	1481.665	1481.5425 ± 0.0022	-1.3 ± 0.4	63.3 ± 0.9	11.4 ± 0.9	
S I	1481.712	1481.5989 ± 0.0022	0.6 ± 0.4	15.7 ± 0.9	11.8 ± 0.9	
C I	1481.764	1481.6572 ± 0.0017	1.8 ± 0.4	27.3 ± 1.4	18.0 ± 0.7	
Ni II	1482.393	1482.2784 ± 0.0019	0.3 ± 0.4	5.2 ± 1.2	15.3 ± 0.9	
		1482.3843 ± 0.0044		1.6 ± 0.2	2.9 ± 1.7	Sandlin-1 1482.45
C I	1482.730	1482.6036 ± 0.0026	-2.1 ± 0.5	4.2 ± 0.6	8.2 ± 1.0	
S I	1483.038	1482.9237 ± 0.0019	0.4 ± 0.4	44.6 ± 1.1	14.7 ± 0.8	
S I	1483.233	1483.1191 ± 0.0021	0.4 ± 0.4	20.6 ± 1.0	12.6 ± 0.8	
S I	1485.622	1485.5024 ± 0.0023	-0.7 ± 0.5	33.4 ± 0.8	10.2 ± 0.9	
N IV	1486.496	1486.4081 ± 0.0049	5.7 ± 1.0	65.2 ± 4.0	45.2 ± 4.2	
		1486.6060 ± 0.0016		7.6 ± 1.8	22.9 ± 0.6	Sandlin-1 1486.68
S I	1487.150	1487.0336 ± 0.0021	-0.0 ± 0.4	21.1 ± 1.0	12.8 ± 0.8	
C I + Fe II	1492.570/.577	1492.4517 ± 0.0037		8.8 ± 1.6	20.7 ± 1.6	
C I	1492.738	1492.6245 ± 0.0019	0.7 ± 0.4	18.9 ± 1.2	15.3 ± 0.8	
C I	1493.273	1493.1698 ± 0.0068	2.7 ± 1.4	5.2 ± 1.0	12.9 ± 1.5	
C I	1494.530	1494.4069 ± 0.0021	-1.3 ± 0.4	7.1 ± 1.0	12.8 ± 2.2	
		1499.7015 ± 0.0152		2.7 ± 1.5	15.8 ± 11.7	Sandlin-1 1499.809
Ni II	1500.437	1500.3325 ± 0.0017	2.6 ± 0.3	23.9 ± 1.6	20.2 ± 0.7	
		1501.4036 ± 0.0022		2.1 ± 0.9	11.7 ± 0.9	
Ni II	1501.962	1501.8534 ± 0.0021	1.8 ± 0.4	6.1 ± 1.0	13.3 ± 0.8	
Ni II	1502.150	1502.0273 ± 0.0015	-1.0 ± 0.3	16.1 ± 1.9	24.1 ± 0.6	
		1502.7277 ± 0.0230		4.1 ± 2.9	23.7 ± 25.8	Sandlin-3 1502.82
		1505.6046 ± 0.0023		1.5 ± 0.8	10.8 ± 2.2	Sandlin-1 1505.73
Fe II	1506.898	1506.7947 ± 0.0025	2.9 ± 0.5	1.1 ± 0.7	8.9 ± 2.1	
		1507.0273 ± 0.0058		5.9 ± 3.8	48.9 ± 28.5	Sandlin-1 1507.13
		1510.0664 ± 0.0023		3.6 ± 0.8	10.4 ± 0.9	Sandlin-3 1510.17
C I + H ₂	1510.668/.693	1510.5520 ± 0.0024		6.0 ± 0.8	9.8 ± 0.9	
Ni II	1510.859	1510.7473 ± 0.0018	1.3 ± 0.4	32.3 ± 1.3	16.8 ± 0.7	
C I	1510.981	1510.8629 ± 0.0021	0.0 ± 0.4	29.4 ± 1.0	13.0 ± 0.8	
C I	1511.907	1511.7831 ± 0.0023	-1.1 ± 0.5	6.4 ± 0.8	11.0 ± 0.9	
C I	1513.150	1513.0364 ± 0.0022	0.9 ± 0.4	7.7 ± 0.9	12.2 ± 0.8	
Si I	1521.415	1521.2809 ± 0.0017	-3.0 ± 0.3	8.2 ± 1.5	20.1 ± 0.7	
Si I	1522.983	1522.8496 ± 0.0026	-2.8 ± 0.5	2.6 ± 0.7	8.5 ± 1.0	
Si I	1523.109	1522.9854 ± 0.0036	-0.9 ± 0.7	1.4 ± 0.3	4.4 ± 2.8	

Table 4—Continued

Line ^a ID	Lab Wavelength (Å)	Observed Wavelength (Å)	Velocity ^b Shift km s ⁻¹	Flux (10 ⁻¹⁵) erg cm ⁻² s ⁻¹	FWHM ^c km s ⁻¹	Notes ^d
Si I + Si I	1523.200/.259	1523.1406 ± 0.0022		5.8 ± 0.9	12.2 ± 0.8	
Fe II	1523.374	1523.2538 ± 0.0023	-0.2 ± 0.5	12.2 ± 0.8	10.9 ± 0.9	
Si I + Si I	1523.543/.568	1523.4457 ± 0.0018		9.2 ± 1.4	17.6 ± 0.7	
Si I	1523.915	1523.7922 ± 0.0014	-0.7 ± 0.3	19.5 ± 2.3	30.2 ± 0.5	
Si I	1524.316	1524.1754 ± 0.0015	-4.2 ± 0.3	11.5 ± 1.9	25.0 ± 0.6	
Si I	1524.767	1524.6510 ± 0.0013	0.6 ± 0.3	20.7 ± 2.6	33.6 ± 0.5	
H ₂ + Ca II	1525.230/.232	1525.1401 ± 0.0015		14.0 ± 1.9	25.2 ± 0.6	
Si I + Si I	1525.832/.886	1525.7616 ± 0.0012		25.0 ± 3.3	43.1 ± 0.5	
Si I	1526.549	1526.4170 ± 0.0021	-2.5 ± 0.4	27.6 ± 1.1	13.7 ± 0.8	
Si II	1526.708	1526.5884 ± 0.0013	-0.0 ± 0.3	273.9 ± 2.5	32.8 ± 0.5	emd, ISM, CR
		1526.7761 ± 0.0029		2.5 ± 0.5	6.8 ± 1.1	Sandlin-1 1526.89
Si I	1527.223	1527.0840 ± 0.0018	-3.8 ± 0.3	8.2 ± 1.5	18.9 ± 0.7	Kelly (1982)
Si I + Si I	1527.343/.367	1527.2533 ± 0.0018		37.2 ± 1.5	19.0 ± 0.7	
Si I	1527.588	1527.4590 ± 0.0014	-1.9 ± 0.3	18.6 ± 2.4	30.9 ± 0.5	Kelly (1982)
Si I + Si I	1527.989/8.072	1527.9086 ± 0.0014		10.6 ± 2.4	30.8 ± 0.5	
Si I	1528.372	1528.2552 ± 0.0028	0.6 ± 0.5	4.9 ± 0.6	7.6 ± 1.1	
		1528.4706 ± 0.0026		4.3 ± 0.7	8.6 ± 1.0	
CO + Si I	1528.860/.871	1528.7402 ± 0.0028		4.2 ± 0.6	7.4 ± 1.1	
Si I + Si I	1529.022/.061	1528.9084 ± 0.0020		9.7 ± 1.1	14.8 ± 0.8	
Si I	1529.202	1529.0876 ± 0.0028	1.0 ± 0.5	11.1 ± 1.4	13.1 ± 1.4	
Si I	1529.396	1529.2640 ± 0.0066	-2.4 ± 1.3	12.9 ± 1.3	17.5 ± 0.7	
Si I	1529.532	1529.4156 ± 0.0023	0.6 ± 0.4	9.0 ± 3.0	11.4 ± 1.9	
Si I	1529.778	1529.6570 ± 0.0029	-0.3 ± 0.6	5.2 ± 0.5	6.8 ± 1.1	
Si I	1529.870	1529.7628 ± 0.0018	2.4 ± 0.4	5.8 ± 1.4	17.6 ± 0.7	
Si I	1530.690	1530.5575 ± 0.0016	-2.5 ± 0.3	13.6 ± 1.7	21.9 ± 0.6	Kelly (1982)
Si I + Si I + Si	1530.867/.875/.929	1530.8220 ± 0.0012		38.4 ± 3.0	38.4 ± 0.5	
Si I	1531.070/.116	1530.9913 ± 0.0018		10.5 ± 1.4	17.6 ± 0.7	
Si I	1531.602	1531.4823 ± 0.0024	0.0 ± 0.5	12.5 ± 0.8	9.9 ± 0.9	
Si I	1532.295	1532.1808 ± 0.0024	1.1 ± 0.5	7.5 ± 0.8	10.5 ± 0.9	
Si I + Si I	1532.446/.490	1532.3580 ± 0.0019		21.7 ± 1.3	16.8 ± 0.7	
Si I + Si I	1532.624/.646	1532.5237 ± 0.0020		24.5 ± 1.1	14.2 ± 0.8	
Si I	1532.815	1532.6725 ± 0.0024	-4.4 ± 0.5	8.7 ± 0.8	10.1 ± 0.9	
Si I	1532.929	1532.7997 ± 0.0018	-1.8 ± 0.3	14.1 ± 1.5	19.1 ± 0.7	
Si I	1533.036	1532.9202 ± 0.0022	0.8 ± 0.4	6.7 ± 0.9	11.7 ± 0.9	
Si II	1533.432	1533.3102 ± 0.0013	-0.4 ± 0.2	301.3 ± 2.9	37.1 ± 0.5	emd, CR
Si I + Si I	1533.672/.717	1533.5780 ± 0.0021		13.1 ± 1.0	13.6 ± 0.8	
Si I	1534.112	1533.9861 ± 0.0026	-1.2 ± 0.5	10.2 ± 0.7	8.9 ± 1.0	
Si I	1534.184	1534.0667 ± 0.0021	0.5 ± 0.4	20.4 ± 1.0	13.2 ± 0.8	
Si I	1534.431	1534.2938 ± 0.0019	-3.4 ± 0.4	8.5 ± 1.3	16.7 ± 0.7	
Si I	1534.547	1534.4333 ± 0.0023	1.2 ± 0.4	5.1 ± 0.9	11.6 ± 0.9	
Si I	1534.707	1534.5811 ± 0.0024	-1.2 ± 0.5	11.3 ± 0.8	10.1 ± 0.9	
H ₂ + Si I	1534.772/.778	1534.6583 ± 0.0018		26.4 ± 1.4	18.2 ± 0.7	
Si I	1534.996	1534.8721 ± 0.0021	-0.7 ± 0.4	13.0 ± 1.1	13.8 ± 0.8	
Si I	1535.472	1535.3364 ± 0.0044	-3.0 ± 0.9	2.4 ± 0.2	3.0 ± 1.7	
Si I + P II	1535.896/.90	1535.7749 ± 0.0024		7.2 ± 0.8	10.4 ± 0.9	
Si I	1536.085	1535.9624 ± 0.0026	-0.5 ± 0.5	14.3 ± 0.7	9.1 ± 1.0	
Si I + Si I	1536.257/.285	1536.1758 ± 0.0018		11.7 ± 1.4	18.7 ± 0.7	
Si I	1536.473	1536.3719 ± 0.0022	3.7 ± 0.4	5.8 ± 1.0	12.6 ± 0.8	
Ni II	1536.746	1536.6345 ± 0.0019	1.7 ± 0.4	23.8 ± 1.3	16.5 ± 0.7	
Si I + Ni II	1537.016/.038	1536.9221 ± 0.0010		41.7 ± 4.2	54.0 ± 0.4	
Si I	1537.297	1537.1759 ± 0.0025	-0.2 ± 0.5	21.9 ± 0.7	9.4 ± 1.0	

Table 4—Continued

Line ^a ID	Lab Wavelength (Å)	Observed Wavelength (Å)	Velocity ^b Shift km s ⁻¹	Flux (10 ⁻¹⁵) erg cm ⁻² s ⁻¹	FWHM ^c km s ⁻¹	Notes ^d
Si I	1537.474	1537.3624 ± 0.0021	1.7 ± 0.4	23.9 ± 1.0	13.0 ± 0.8	
Si I	1537.618	1537.4952 ± 0.0023	-0.5 ± 0.5	17.7 ± 0.8	11.0 ± 0.9	
Si I	1537.935	1537.8163 ± 0.0025	0.3 ± 0.5	24.6 ± 0.8	9.8 ± 0.9	
Si I	1538.876	1538.7573 ± 0.0023	0.3 ± 0.4	10.2 ± 0.9	11.4 ± 0.9	
Si I	1539.236	1539.1089 ± 0.0025	-1.3 ± 0.5	3.5 ± 0.7	9.4 ± 1.0	
Si I	1539.705	1539.5776 ± 0.0025	-1.3 ± 0.5	6.1 ± 0.8	9.8 ± 0.9	
Si I	1540.286	1540.1740 ± 0.0023	1.6 ± 0.4	8.4 ± 0.9	11.7 ± 0.9	
Si I	1540.544	1540.4131 ± 0.0022	-2.0 ± 0.4	9.9 ± 0.9	12.0 ± 0.9	
Si I	1540.707	1540.5852 ± 0.0025	-0.3 ± 0.5	18.0 ± 0.7	9.2 ± 1.0	
Si I	1540.783	1540.6580 ± 0.0023	-0.9 ± 0.4	29.7 ± 0.9	11.6 ± 0.9	
Si I	1540.963	1540.8365 ± 0.0023	-1.2 ± 0.5	27.2 ± 0.8	10.8 ± 0.9	
Si I	1541.322	1541.2021 ± 0.0022	0.1 ± 0.4	22.4 ± 1.0	12.6 ± 0.8	
Si I	1541.397	1541.2899 ± 0.0025	2.6 ± 0.5	10.4 ± 0.8	9.8 ± 0.9	
Si I	1541.569	1541.4443 ± 0.0017	-0.8 ± 0.3	22.0 ± 1.6	20.6 ± 0.7	
C I	1542.177	1542.0541 ± 0.0021	-0.4 ± 0.4	47.1 ± 1.1	13.7 ± 0.8	
Si I	1542.432	1542.3113 ± 0.0027	-0.0 ± 0.5	11.7 ± 0.6	8.0 ± 1.0	
Si I	1543.158	1543.0129 ± 0.0023	-4.7 ± 0.4	3.1 ± 0.9	11.4 ± 0.9	
Si I	1543.724	1543.6051 ± 0.0024	0.4 ± 0.5	27.2 ± 0.8	10.4 ± 0.9	
C I	1543.960	1543.8351 ± 0.0022	-0.8 ± 0.4	15.6 ± 0.9	12.3 ± 0.8	
Si I	1544.184	1544.0663 ± 0.0024	0.6 ± 0.5	13.6 ± 0.8	10.1 ± 0.9	
Si I	1544.591	1544.4712 ± 0.0022	0.2 ± 0.4	16.5 ± 0.9	11.9 ± 0.9	
Si I	1545.099	1544.9655 ± 0.0159	-2.5 ± 3.1	23.4 ± 11.8	21.5 ± 11.8	
CO + C I	1545.210/.249	1545.1069 ± 0.0016		24.7 ± 1.9	24.4 ± 0.6	
Si I	1545.575	1545.4552 ± 0.0023	0.2 ± 0.5	39.3 ± 0.8	10.9 ± 0.9	
Si I	1545.749	1545.6274 ± 0.0023	-0.1 ± 0.5	15.9 ± 0.8	11.0 ± 0.9	
Si I	1546.590	1546.4673 ± 0.0027	-0.3 ± 0.5	11.5 ± 0.7	8.5 ± 1.0	
Si I	1546.674	1546.5448 ± 0.0023	-1.6 ± 0.4	18.4 ± 0.9	11.1 ± 0.9	
Si I	1547.129	1547.0166 ± 0.0024	1.7 ± 0.5	10.2 ± 0.8	10.2 ± 0.9	
H ₂ + Si I	1547.337/.362	1547.2428 ± 0.0024		19.2 ± 0.8	10.2 ± 0.9	
Si I	1547.452	1547.3308 ± 0.0024	-0.0 ± 0.5	15.0 ± 0.8	10.2 ± 0.9	
Si I	1547.731	1547.6090 ± 0.0037	-0.2 ± 0.7	2.7 ± 0.3	4.4 ± 1.4	
Fe II	1547.807	1547.6777 ± 0.0026	-1.6 ± 0.5	6.2 ± 0.7	9.1 ± 1.0	
C IV	1548.187	1548.1071 ± 0.0011	8.0 ± 0.2	1800.0 ± 3.7	48.6 ± 0.4	NC+BC,ISM,NIST
Si I	1548.715	1548.5922 ± 0.0018	-0.3 ± 0.4	48.8 ± 1.4	17.6 ± 0.7	
		1548.9562 ± 0.0022		10.3 ± 1.0	12.4 ± 0.8	Sandlin-1 1549.05
Si I	1549.536	1549.4138 ± 0.0048	-0.2 ± 0.9	2.3 ± 0.2	UL	
Fe II	1550.260	1550.1577 ± 0.0017	3.7 ± 0.3	51.2 ± 1.5	20.1 ± 0.7	
C IV	1550.772	1550.6807 ± 0.0011	5.8 ± 0.2	998.0 ± 4.0	52.0 ± 0.4	NC+BC,NIST
Si I	1551.240	1551.1228 ± 0.0023	0.8 ± 0.4	41.8 ± 0.9	11.5 ± 0.9	
Si I	1551.860	1551.7306 ± 0.0025	-1.5 ± 0.5	31.8 ± 0.8	9.8 ± 0.9	
Si I	1551.930	1551.8030 ± 0.0018	-1.1 ± 0.3	28.1 ± 1.4	18.6 ± 0.7	
Si I	1552.209	1552.0868 ± 0.0023	-0.2 ± 0.4	40.5 ± 0.9	11.5 ± 0.9	
		1552.6396 ± 0.0022		13.2 ± 1.0	12.7 ± 0.8	Sandlin 1552.757
Si I + H ₂	1552.950/.958	1552.8254 ± 0.0025		12.0 ± 0.7	9.4 ± 1.0	
Si I	1553.370	1553.2487 ± 0.0024	0.0 ± 0.5	15.7 ± 0.8	10.3 ± 0.9	
Si I	1554.702	1554.5873 ± 0.0023	1.3 ± 0.4	25.0 ± 0.9	11.5 ± 0.9	
Si I	1555.516	1555.3906 ± 0.0020	-0.7 ± 0.4	15.0 ± 1.2	15.2 ± 0.8	
Si I	1555.660	1555.5422 ± 0.0023	0.7 ± 0.4	15.0 ± 0.9	11.5 ± 0.9	
Si I+Fe IV+Ni II	1555.946/.950/.957	1555.8601 ± 0.0019		6.9 ± 1.3	16.6 ± 0.7	
Si I	1556.160	1556.0364 ± 0.0025	-0.4 ± 0.5	22.8 ± 0.7	9.7 ± 1.0	
Si I + Si I	1556.527/.547	1556.4149 ± 0.0021		26.4 ± 1.1	14.0 ± 0.8	

Table 4—Continued

Line ^a ID	Lab Wavelength (Å)	Observed Wavelength (Å)	Velocity ^b Shift km s ⁻¹	Flux (10 ⁻¹⁵) erg cm ⁻² s ⁻¹	FWHM ^c km s ⁻¹	Notes ^d
CO + Si I	1557.380/.382	1556.9186 ± 0.0034		7.7 ± 0.4	5.2 ± 1.3	Sandlin-1 1557.044
		1557.2502 ± 0.0019		13.1 ± 1.2	16.1 ± 0.7	
		1557.4197 ± 0.0020		7.5 ± 1.2	15.7 ± 2.0	Sandlin-1 1557.53
		1557.7454 ± 0.0018		6.7 ± 1.4	18.2 ± 0.7	Sandlin-1 1557.86
Si I	1558.240	1558.1143 ± 0.0023	-0.7 ± 0.4	24.6 ± 0.9	11.3 ± 0.9	
Fe II	1558.542	1558.4161 ± 0.0017	-0.8 ± 0.3	56.7 ± 1.6	20.6 ± 0.7	
Fe II	1558.690	1558.5800 ± 0.0015	2.3 ± 0.3	81.5 ± 2.1	27.6 ± 0.6	
Fe II	1559.084	1558.9678 ± 0.0014	1.1 ± 0.3	193.7 ± 2.4	30.9 ± 0.5	
		1559.1445 ± 0.0028		5.4 ± 0.6	7.9 ± 1.1	
Si I	1559.364	1559.2352 ± 0.0022	-1.3 ± 0.4	32.4 ± 0.9	12.2 ± 0.8	
Si I	1559.705	1559.5873 ± 0.0025	0.8 ± 0.5	11.5 ± 0.8	9.9 ± 0.9	
Si I	1560.072	1559.9551 ± 0.0022	1.0 ± 0.4	43.2 ± 1.0	12.8 ± 0.8	
C I	1560.310	1560.1909 ± 0.0015	0.6 ± 0.3	209.0 ± 4.4	27.6 ± 0.6	CR
C I + C I	1560.683/.708	1560.5730 ± 0.0014		243.1 ± 6.8	30.2 ± 0.5	CR
Ni II	1561.015	1560.8961 ± 0.0024	0.6 ± 0.5	4.8 ± 0.8	10.7 ± 0.9	
Fe II	1561.067	1560.9480 ± 0.0033	0.6 ± 0.6	10.1 ± 0.4	5.6 ± 1.2	
C I + C I + C I	1561.341/.367/.438	1561.2780 ± 0.0010		340.3 ± 4.3	56.0 ± 0.4	CR
Si I	1561.822	1561.6981 ± 0.0026	-0.3 ± 0.5	20.1 ± 0.7	8.7 ± 1.0	
Si I + Si I	1562.002/.006	1561.8812 ± 0.0024		28.9 ± 0.8	11.0 ± 0.9	
Si I	1562.286	1562.1493 ± 0.0019	-2.8 ± 0.4	18.9 ± 1.3	16.6 ± 0.7	
Si I	1563.364	1563.2338 ± 0.0024	-1.5 ± 0.5	14.9 ± 0.8	10.8 ± 0.9	
Fe II	1563.788	1563.6748 ± 0.0015	1.8 ± 0.3	171.2 ± 2.2	28.9 ± 0.6	
Al IV	1564.164	1564.0623 ± 0.0035	4.0 ± 0.7	3.4 ± 0.4	5.1 ± 1.3	NIST
Si I	1564.614	1564.4858 ± 0.0022	-1.1 ± 0.4	39.3 ± 1.0	13.1 ± 0.8	
H ₂	1565.232	1565.1031 ± 0.0026	-1.2 ± 0.5	3.2 ± 0.7	9.2 ± 1.0	
Si I + Si I	1565.322/.395	1565.2421 ± 0.0019		28.7 ± 1.3	16.6 ± 0.7	
		1565.3983 ± 0.0028		4.6 ± 0.6	8.0 ± 1.0	Sandlin-1 1565.52
Fe II	1566.819	1566.7079 ± 0.0016	2.2 ± 0.3	123.2 ± 1.9	25.1 ± 0.6	
Si I	1567.465	1567.3174 ± 0.0024	-4.8 ± 0.5	5.4 ± 0.8	10.7 ± 0.9	
		1567.4459 ± 0.0026		5.1 ± 0.7	9.0 ± 1.0	Sandlin-1 1567.576
Si I	1567.726	1567.6029 ± 0.0025	-0.1 ± 0.5	16.1 ± 0.8	10.2 ± 0.9	
Fe II	1568.016	1567.9043 ± 0.0018	2.1 ± 0.3	65.1 ± 1.5	19.5 ± 0.7	
Si I	1568.196	1568.0742 ± 0.0023	0.2 ± 0.4	29.3 ± 0.9	11.4 ± 0.9	
Si I	1568.618	1568.5015 ± 0.0023	1.2 ± 0.4	13.1 ± 0.9	11.9 ± 0.9	
Si I	1569.319	1569.1970 ± 0.0024	0.2 ± 0.5	21.3 ± 0.8	10.8 ± 0.9	
Fe II	1569.674	1569.5615 ± 0.0016	2.0 ± 0.3	96.0 ± 1.7	22.7 ± 0.6	
Si I	1570.027	1569.8998 ± 0.0025	-0.8 ± 0.5	11.4 ± 0.8	10.2 ± 0.9	
Fe II	1570.242	1570.1281 ± 0.0016	1.7 ± 0.3	141.1 ± 1.8	23.8 ± 0.6	
Si I	1570.517	1570.3961 ± 0.0020	0.4 ± 0.4	16.0 ± 1.2	15.1 ± 0.8	
Si I + Ni II	1570.810/.878	1570.7087 ± 0.0017		8.0 ± 1.6	20.4 ± 0.7	
Fe II	1571.137	1571.0139 ± 0.0022	-0.0 ± 0.4	46.4 ± 1.0	12.9 ± 0.8	
Si I	1571.406	1571.2794 ± 0.0019	-0.7 ± 0.4	38.9 ± 1.3	16.5 ± 0.7	
		1571.4072 ± 0.0024		5.7 ± 0.8	10.8 ± 0.9	Sandlin-1 1571.55
Si I	1571.796	1571.6766 ± 0.0020	0.7 ± 0.4	19.9 ± 1.2	15.6 ± 0.7	
		1572.0121 ± 0.0019		7.2 ± 1.3	17.0 ± 0.7	
		1572.3070 ± 0.0017		8.9 ± 1.6	21.0 ± 0.6	
Ni II	1572.646	1572.5190 ± 0.0030	-0.8 ± 0.6	7.8 ± 0.5	7.0 ± 1.1	
Si I + Fe II	1572.717/.750	1572.6188 ± 0.0015		36.0 ± 2.1	27.5 ± 0.6	
Fe II	1573.000	1572.8910 ± 0.0017	2.7 ± 0.3	16.3 ± 1.7	22.6 ± 0.6	
		1573.3136 ± 0.0021		6.5 ± 1.1	14.2 ± 0.8	Sandlin-1 1573.44
Si I	1573.635	1573.5109 ± 0.0022	-0.2 ± 0.4	45.8 ± 1.0	12.9 ± 0.8	

Table 4—Continued

Line ^a ID	Lab Wavelength (Å)	Observed Wavelength (Å)	Velocity ^b Shift km s ⁻¹	Flux (10 ⁻¹⁵) erg cm ⁻² s ⁻¹	FWHM ^c km s ⁻¹	Notes ^d
Fe II	1573.825	1573.6866 ± 0.0021	-2.9 ± 0.4	39.8 ± 1.0	13.4 ± 0.8	
Si I	1573.884	1573.7612 ± 0.0022	0.1 ± 0.4	61.3 ± 1.0	12.9 ± 0.8	
		1574.4445 ± 0.0023		14.3 ± 0.9	11.3 ± 0.9	Sandlin-1 1574.544
Fe II	1574.768	1574.6482 ± 0.0018	0.7 ± 0.3	35.6 ± 1.5	20.0 ± 0.7	
Fe II+Ni II	1574.923/.976/5.003	1574.7968 ± 0.0048		199.5 ± 11.6	37.7 ± 1.4	
Si I	1575.127	1575.0049 ± 0.0025	0.2 ± 0.5	23.0 ± 1.3	10.2 ± 0.9	
Si I	1576.825	1576.6951 ± 0.0023	-1.2 ± 0.4	24.5 ± 0.9	11.7 ± 0.9	
Si I	1577.044	1576.9181 ± 0.0028	-0.5 ± 0.5	6.2 ± 0.6	7.7 ± 1.1	
Fe II	1577.166	1577.0435 ± 0.0018	0.2 ± 0.3	62.5 ± 1.5	19.0 ± 0.7	
Fe II	1578.219	1578.1040 ± 0.0026	1.6 ± 0.5	8.0 ± 0.7	9.0 ± 1.0	
Si I + Fe II	1578.478/.495	1578.3770 ± 0.0021		34.2 ± 1.0	13.6 ± 0.8	
Si I	1580.300	1580.1733 ± 0.0024	-0.6 ± 0.5	16.5 ± 0.8	10.9 ± 0.9	
Fe II	1580.625	1580.5162 ± 0.0017	2.8 ± 0.3	120.8 ± 1.8	22.9 ± 0.6	
Fe II	1581.274	1581.1536 ± 0.0023	0.6 ± 0.4	38.0 ± 0.9	11.5 ± 0.9	
Fe I	1583.600	1583.4723 ± 0.0027	-0.7 ± 0.5	13.6 ± 0.6	8.4 ± 1.0	Kelly (1982)
Fe IV	1584.117	1584.0118 ± 0.0024	3.6 ± 0.4	8.9 ± 0.9	11.2 ± 0.9	Kelly (1982)
		1584.1162 ± 0.0024		10.8 ± 0.8	10.9 ± 0.9	
Si I	1584.346	1584.2223 ± 0.0024	0.1 ± 0.5	19.9 ± 0.8	10.7 ± 0.9	
Fe II	1584.949	1584.8344 ± 0.0016	1.8 ± 0.3	112.9 ± 1.8	23.6 ± 0.6	
Fe II	1585.999	1585.8878 ± 0.0018	2.4 ± 0.3	19.6 ± 1.4	18.4 ± 0.7	
Si I	1586.137	1586.0048 ± 0.0025	-1.5 ± 0.5	9.1 ± 0.7	9.7 ± 1.0	
Si I	1586.791	1586.6700 ± 0.0023	0.6 ± 0.4	12.0 ± 0.9	11.4 ± 0.9	
Si I	1587.762	1587.6406 ± 0.0024	0.5 ± 0.5	13.0 ± 0.8	10.9 ± 0.9	
Fe II	1588.286	1588.1697 ± 0.0017	1.5 ± 0.3	147.8 ± 1.7	21.9 ± 0.6	
Fe II	1588.688	1588.5590 ± 0.0024	-0.9 ± 0.4	20.5 ± 0.9	11.2 ± 0.9	
H ₂ + Si I	1589.153/.173	1589.0321 ± 0.0027		6.8 ± 0.7	8.9 ± 1.0	
		1590.0020 ± 0.0024		24.9 ± 0.8	10.8 ± 0.9	Sandlin-1 1590.10
Si I	1590.477	1590.3448 ± 0.0017	-1.5 ± 0.3	18.4 ± 1.8	22.9 ± 0.6	
Si I	1590.576	1590.4575 ± 0.0033	1.1 ± 0.6	6.5 ± 0.5	5.9 ± 1.2	
Fe IV	1590.863	1590.7412 ± 0.0025	0.5 ± 0.5	5.2 ± 0.8	9.9 ± 0.9	Kelly (1982)
Si I	1591.123	1590.9769 ± 0.0029	-4.1 ± 0.5	9.6 ± 0.6	7.6 ± 1.1	
Fe IV	1591.509	1591.3608 ± 0.0026	-4.5 ± 0.5	4.0 ± 0.7	9.3 ± 1.0	Kelly (1982)
Si I	1592.020	1591.8876 ± 0.0027	-1.5 ± 0.5	5.7 ± 0.7	8.7 ± 1.0	
Si I	1592.423	1592.2952 ± 0.0026	-0.6 ± 0.5	39.7 ± 0.7	9.7 ± 1.0	
Si I	1594.566	1594.4390 ± 0.0024	-0.4 ± 0.5	49.3 ± 0.8	11.0 ± 0.9	
Si I + Si I	1594.949/.951	1594.8247 ± 0.0022		48.2 ± 1.0	13.1 ± 0.8	
Si I	1595.755	1595.6283 ± 0.0022	-0.4 ± 0.4	26.5 ± 1.0	12.7 ± 0.8	
Si I	1597.720	1597.5842 ± 0.0031	-2.0 ± 0.6	6.6 ± 0.5	6.6 ± 1.2	
Si I	1597.962	1597.8450 ± 0.0018	1.5 ± 0.3	37.7 ± 1.5	19.5 ± 0.7	
		1598.0725 ± 0.0036		4.7 ± 0.4	5.1 ± 1.3	Sandlin-1 1598.19
Fe II	1598.455	1598.3361 ± 0.0017	1.2 ± 0.3	16.9 ± 1.7	21.8 ± 0.6	
		1598.9319 ± 0.0020		9.1 ± 1.3	16.8 ± 0.7	Sandlin-1 1599.07
Fe II	1600.013	1599.8939 ± 0.0027	1.1 ± 0.5	25.5 ± 0.7	8.7 ± 1.0	
Ni II	1600.268	1600.1565 ± 0.0026	2.6 ± 0.5	14.1 ± 0.7	9.4 ± 1.0	
C I	1600.818	1600.6877 ± 0.0026	-0.9 ± 0.5	7.7 ± 0.8	9.8 ± 0.9	
CO	1600.940	1600.8009 ± 0.0026	-2.6 ± 0.5	25.5 ± 0.7	9.6 ± 1.0	
CO	1601.230	1601.1184 ± 0.0022	2.6 ± 0.4	15.2 ± 1.1	13.8 ± 0.8	
Fe IV	1601.826	1601.6906 ± 0.0026	-1.9 ± 0.5	7.0 ± 0.7	9.2 ± 1.0	Kelly (1982)
Cl II	1602.010	1601.8856 ± 0.0028	0.2 ± 0.5	17.6 ± 0.6	8.4 ± 1.0	Kelly (1982)
Fe II	1602.210	1602.0900 ± 0.0018	1.0 ± 0.3	50.4 ± 1.9	20.2 ± 0.7	
		1602.4025 ± 0.0018		87.3 ± 1.5	19.1 ± 0.7	

Table 4—Continued

Line ^a ID	Lab Wavelength (Å)	Observed Wavelength (Å)	Velocity ^b Shift km s ⁻¹	Flux (10 ⁻¹⁵) erg cm ⁻² s ⁻¹	FWHM ^c km s ⁻¹	Notes ^d
		1602.5874 ± 0.0024		4.8 ± 0.9	11.1 ± 0.9	
C I	1602.972	1602.8510 ± 0.0021	0.8 ± 0.4	52.7 ± 1.2	15.3 ± 0.8	
Fe II	1604.583	1604.4462 ± 0.0023	-2.1 ± 0.4	9.6 ± 0.9	11.7 ± 0.9	
Fe II	1605.318	1605.2067 ± 0.0025	2.7 ± 0.5	21.0 ± 0.8	10.4 ± 0.9	
Ni II + C I	1606.917/.960	1606.8337 ± 0.0025		18.1 ± 0.8	10.2 ± 0.9	
C I + Fe II	1608.438/.456	1608.3516 ± 0.0014		120.5 ± 2.4	31.3 ± 0.5	
Fe II	1610.921	1610.8033 ± 0.0017	1.6 ± 0.3	128.3 ± 1.8	23.4 ± 0.6	
Fe II	1611.201	1611.0746 ± 0.0019	-0.1 ± 0.4	83.9 ± 1.4	17.8 ± 0.7	
Fe II	1612.802	1612.6881 ± 0.0016	2.3 ± 0.3	160.5 ± 2.1	26.7 ± 0.6	
		1612.9030 ± 0.0022		13.1 ± 1.0	13.5 ± 0.8	Sandlin-1 1613.02
C I	1613.376	1613.2455 ± 0.0023	-0.8 ± 0.4	71.5 ± 0.9	12.2 ± 0.8	
C I	1613.803	1613.6770 ± 0.0023	0.0 ± 0.4	69.5 ± 1.0	12.4 ± 0.8	
C I	1614.507	1614.3784 ± 0.0022	-0.4 ± 0.4	79.0 ± 1.0	13.1 ± 0.8	
Fe II	1616.652	1616.5317 ± 0.0021	1.2 ± 0.4	44.7 ± 1.1	14.4 ± 0.8	
Fe II	1618.470	1618.3435 ± 0.0016	0.0 ± 0.3	100.8 ± 1.9	24.8 ± 0.6	
Fe II + Fe II	1618.955/.961	1618.8680 ± 0.0028		11.2 ± 0.7	8.6 ± 1.0	
Fe II	1620.061	1619.9468 ± 0.0022	2.3 ± 0.4	28.6 ± 1.1	13.8 ± 0.8	
Ni II	1620.331	1620.2047 ± 0.0013	0.1 ± 0.2	27.3 ± 3.1	39.9 ± 0.5	
Fe II	1621.252	1621.1321 ± 0.0020	1.3 ± 0.4	51.0 ± 1.3	16.4 ± 0.7	
Fe II	1621.685	1621.5604 ± 0.0016	0.4 ± 0.3	40.6 ± 2.0	25.5 ± 0.6	
Fe II	1621.867	1621.7515 ± 0.0022	2.1 ± 0.4	67.8 ± 1.0	13.6 ± 0.8	
Si I	1622.881	1622.7548 ± 0.0020	0.1 ± 0.4	26.1 ± 1.3	17.0 ± 0.7	
Fe II	1623.091	1622.9700 ± 0.0016	1.1 ± 0.3	115.5 ± 1.9	24.9 ± 0.6	
Fe II	1623.705	1623.5789 ± 0.0020	0.2 ± 0.4	47.2 ± 1.2	15.8 ± 0.7	
Fe II	1625.520	1625.4011 ± 0.0016	1.5 ± 0.3	190.9 ± 2.1	27.1 ± 0.6	
Fe II	1625.909	1625.7876 ± 0.0019	1.1 ± 0.4	83.4 ± 1.4	17.8 ± 0.7	
Fe II	1627.130	1627.0128 ± 0.0025	1.9 ± 0.5	26.1 ± 0.8	10.7 ± 0.9	
Fe II	1627.382	1627.2643 ± 0.0020	1.8 ± 0.4	74.7 ± 1.3	16.9 ± 0.7	
Fe II	1628.722	1628.6051 ± 0.0024	1.9 ± 0.4	12.5 ± 0.9	11.5 ± 0.9	
Fe II	1629.154	1629.0222 ± 0.0016	-0.8 ± 0.3	50.6 ± 2.0	26.0 ± 0.6	
Fe II+Si I+Si I	1629.376/.404/.438	1629.2841 ± 0.0018		53.1 ± 1.6	20.5 ± 0.7	
Fe II	1629.948	1629.8147 ± 0.0023	-1.1 ± 0.4	37.4 ± 1.5	12.2 ± 0.9	
Fe II	1631.120	1630.9895 ± 0.0016	-0.5 ± 0.3	36.0 ± 2.0	26.6 ± 0.6	
Fe II	1632.307	1632.1735 ± 0.0021	-1.1 ± 0.4	43.8 ± 1.1	14.8 ± 0.8	
Fe II	1632.668	1632.5454 ± 0.0018	0.9 ± 0.3	152.3 ± 1.6	20.7 ± 0.7	
Fe II	1633.908	1633.7960 ± 0.0016	2.9 ± 0.3	150.2 ± 2.0	26.4 ± 0.6	
Fe II	1634.345	1634.2269 ± 0.0018	1.8 ± 0.3	50.5 ± 1.5	19.6 ± 0.7	
Ni II	1635.340	1635.2153 ± 0.0026	0.6 ± 0.5	11.6 ± 0.7	9.6 ± 1.0	
Fe II	1636.331	1636.2148 ± 0.0016	2.2 ± 0.3	27.4 ± 2.0	25.8 ± 0.6	
Fe II	1637.397	1637.2806 ± 0.0016	2.2 ± 0.3	199.3 ± 2.0	25.8 ± 0.6	
Si I	1638.282	1638.1654 ± 0.0025	2.1 ± 0.5	12.2 ± 0.8	10.3 ± 0.9	
P I	1638.657	1638.5206 ± 0.0020	-1.5 ± 0.4	11.7 ± 1.3	16.3 ± 0.7	Kelly (1982)
P I	1639.075	1638.9143 ± 0.0040	-5.9 ± 0.7	3.6 ± 0.3	4.3 ± 1.4	Kelly (1982)
Fe II	1640.152	1640.0334 ± 0.0017	1.8 ± 0.3	211.9 ± 2.0	22.4 ± 0.6	
He II	1640.400	1640.2777 ± 0.0011	1.1 ± 0.2	253.1 ± 6.8	52.1 ± 0.6	(f)
P I	1640.723	1640.5986 ± 0.0028	0.7 ± 0.5	14.7 ± 2.4	17.8 ± 1.9	Kelly (1982)
S I + O I	1641.292/.305	1641.1757 ± 0.0024		27.8 ± 0.9	11.2 ± 0.9	NIST
Fe II	1642.496	1642.3752 ± 0.0021	1.4 ± 0.4	36.6 ± 1.2	15.3 ± 0.8	
Fe II	1643.576	1643.4460 ± 0.0018	-0.3 ± 0.3	183.6 ± 1.7	22.0 ± 0.6	
Fe II	1645.016	1644.8940 ± 0.0022	1.2 ± 0.4	56.4 ± 1.1	14.0 ± 0.8	
Fe II	1648.403	1648.2714 ± 0.0026	-0.5 ± 0.5	14.9 ± 0.8	10.0 ± 0.9	

Table 4—Continued

Line ^a ID	Lab Wavelength (Å)	Observed Wavelength (Å)	Velocity ^b Shift km s ⁻¹	Flux (10 ⁻¹⁵) erg cm ⁻² s ⁻¹	FWHM ^c km s ⁻¹	Notes ^d
Fe II	1649.423	1649.2988 ± 0.0017	0.9 ± 0.3	123.0 ± 1.7	22.5 ± 0.6	
Fe II	1653.403	1653.2793 ± 0.0026	1.0 ± 0.5	9.4 ± 1.8	10.1 ± 0.9	
Ni II + Ni II	1653.687/.779	1653.5928 ± 0.0018		38.0 ± 4.2	21.5 ± 1.5	
CO + CO	1653.800/.85	1653.7313 ± 0.0033		13.3 ± 0.8	6.4 ± 1.2	
Fe II	1654.263	1654.1438 ± 0.0019	1.9 ± 0.3	90.1 ± 3.3	18.5 ± 0.7	
Fe II	1654.476	1654.3540 ± 0.0018	1.4 ± 0.3	94.2 ± 3.2	20.0 ± 0.7	
Fe II	1654.670	1654.5380 ± 0.0027	-0.5 ± 0.5	49.8 ± 0.7	9.3 ± 1.0	
C I	1656.266	1656.1218 ± 0.0014	-2.6 ± 0.2	686.5 ± 2.9	37.1 ± 0.5	CR
Fe IV	1656.649	1656.5199 ± 0.0015	0.1 ± 0.3	117.0 ± 2.3	29.8 ± 0.5	Kelly (1982)
C I + C I	1656.928/7.008	1656.8385 ± 0.0011		545.1 ± 4.5	58.4 ± 0.4	CR
C I	1657.380	1657.2523 ± 0.0014	0.4 ± 0.3	614.4 ± 2.7	35.2 ± 0.5	CR
C I	1657.907	1657.7655 ± 0.0016	-2.1 ± 0.3	405.5 ± 2.2	28.4 ± 0.6	CR
C I	1658.122	1657.9967 ± 0.0015	0.8 ± 0.3	496.2 ± 2.3	30.5 ± 0.5	CR
Fe II	1658.401	1658.2783 ± 0.0025	1.3 ± 0.5	37.8 ± 13.5	11.0 ± 2.2	
		1658.4500 ± 0.0018		40.8 ± 1.7	22.2 ± 0.6	
Fe II	1658.771	1658.6545 ± 0.0017	2.4 ± 0.3	205.6 ± 1.9	24.2 ± 0.6	
Fe II	1659.483	1659.3677 ± 0.0016	2.6 ± 0.3	307.8 ± 2.1	27.4 ± 0.6	
O III	1660.803	1660.7052 ± 0.0018	5.8 ± 0.3	70.3 ± 1.6	20.8 ± 0.6	
Fe II	1661.324	1661.1921 ± 0.0020	-0.3 ± 0.4	59.3 ± 1.3	17.1 ± 0.7	
Fe II	1662.369	1662.2347 ± 0.0026	-0.8 ± 0.5	51.1 ± 0.8	10.2 ± 0.9	
Fe II	1663.221	1663.1025 ± 0.0016	2.1 ± 0.3	168.8 ± 2.0	26.6 ± 0.6	
Fe II	1663.697	1663.5721 ± 0.0029	0.9 ± 0.5	19.9 ± 0.6	8.0 ± 1.0	
O III	1666.153	1666.0386 ± 0.0012	2.9 ± 0.2	126.9 ± 3.5	45.2 ± 0.4	
S I	1666.688	1666.5465 ± 0.0020	-2.0 ± 0.4	51.7 ± 1.7	16.8 ± 0.7	
Fe II	1667.913	1667.7634 ± 0.0015	-3.4 ± 0.3	43.1 ± 2.2	29.2 ± 0.6	
		1668.1093 ± 0.0052		6.5 ± 0.2	UL	
Fe II	1669.663	1669.5385 ± 0.0021	1.1 ± 0.4	91.5 ± 1.3	16.5 ± 0.7	
Al II	1670.787	1670.6689 ± 0.0013	2.3 ± 0.2	725.4 ± 3.4	44.1 ± 0.4	ISM, CR
P I	1671.070	1670.9059 ± 0.0027	-6.0 ± 0.5	18.1 ± 0.7	9.3 ± 1.0	
Fe II	1673.462	1673.3394 ± 0.0019	1.5 ± 0.3	94.4 ± 1.5	19.6 ± 0.7	
Fe II	1674.254	1674.1332 ± 0.0018	1.8 ± 0.3	163.3 ± 1.6	20.7 ± 0.7	
Fe II	1674.440	1674.3193 ± 0.0021	1.9 ± 0.4	29.0 ± 1.2	15.3 ± 0.8	
Fe II	1674.716	1674.5833 ± 0.0016	-0.3 ± 0.3	117.7 ± 2.1	27.7 ± 0.6	
Fe II	1676.361	1676.2305 ± 0.0019	0.1 ± 0.3	57.6 ± 1.5	19.7 ± 0.7	
		1676.6241 ± 0.0021		29.5 ± 1.2	16.0 ± 0.7	
Fe II	1676.856	1676.7385 ± 0.0021	2.5 ± 0.4	108.4 ± 1.3	16.4 ± 0.7	
Fe IV	1677.124	1676.9733 ± 0.0031	-3.5 ± 0.5	10.0 ± 0.6	7.4 ± 1.1	Kelly (1982)
		1677.2212 ± 0.0023		23.4 ± 1.0	12.8 ± 0.8	
Fe II	1677.847	1677.7040 ± 0.0024	-2.1 ± 0.4	33.9 ± 1.0	12.6 ± 0.8	
Fe II	1678.629	1678.5144 ± 0.0017	3.0 ± 0.3	36.0 ± 2.0	25.5 ± 0.6	
Fe II	1679.381	1679.2548 ± 0.0021	0.9 ± 0.4	82.1 ± 1.2	15.5 ± 0.8	
Fe II	1679.494	1679.3868 ± 0.0200	4.3 ± 3.6	33.7 ± 1.2	16.0 ± 0.7	
Ni IV	1680.678	1680.5477 ± 0.0026	0.2 ± 0.5	29.9 ± 0.8	10.6 ± 0.9	
Fe II	1681.111	1680.9872 ± 0.0019	1.4 ± 0.3	161.5 ± 1.5	19.2 ± 0.7	
Fe IV	1681.285	1681.1437 ± 0.0016	-1.8 ± 0.3	58.5 ± 2.1	26.8 ± 0.6	Kelly (1982)
Fe II	1683.315	1683.1772 ± 0.0020	-1.1 ± 0.4	44.0 ± 1.3	17.4 ± 0.7	
Fe II	1684.005	1683.8538 ± 0.0017	-3.5 ± 0.3	66.1 ± 1.9	24.7 ± 0.6	
Fe II + Ni II	1685.954/.965	1685.8533 ± 0.0017		119.9 ± 1.8	23.8 ± 0.6	
Fe II	1686.455	1686.3281 ± 0.0017	0.9 ± 0.3	177.5 ± 1.8	23.8 ± 0.6	
Fe II	1686.692	1686.5676 ± 0.0017	1.3 ± 0.3	243.1 ± 1.9	25.0 ± 0.6	

Note. —

^a Line identification is according to Sandlin et al. (1986) unless differently noted in the last column.^b Radial velocity shifts corrected for the stellar radial velocity of -23.45 km s⁻¹, computed using the orbital parameters and ephemeris given by Pourbaix et al. (2002);^c UL means unresolved line;^d CR means line with Central Reversal; ISM means presence of an absorption component due to interstellar medium absorption; emd means that the line was used to derive the differential emission measure distribution; NC and BC means that the line profile can be fit by a broad plus a narrow components. Not identified lines present also in the solar spectrum, and classified by Sandlin et al. (1986) in four classes, are listed with the name *Sandlin-class-number* and the observed wavelength in the Solar spectrum; NIST means that the line has been identified according to the NIST